Ocean Modelling 152 (2020) 101655

Contents lists available at ScienceDirect

Ocean Modelling

journal homepage: www.elsevier.com/locate/ocemod

Impact of ENSO on the South China Sea during ENSO decaying winter–spring modeled by a regional coupled model (a new mesoscale perspective)

Yi-Chun Kuo, Yu-Heng Tseng *

Institute of Oceanography, National Taiwan University, Taipei, Taiwan

ARTICLE INFO

Keywords:
Regional coupled model
South China sea
ENSO

ABSTRACT

Studies have suggested that the ocean dynamics in the South China Sea (SCS) play a crucial role in local air–sea processes and the regional weather or climate system. We used a high-resolution regional coupled model to investigate the impact of the El Niño Southern Oscillation (ENSO) on the atmospheric and oceanic processes in the SCS during ENSO decaying winter–spring. The coupled model demonstrates the important roles of mesoscale features in the regional air–sea interaction induced by the anomalous ENSO conditions. During El Niño, the Kuroshio intrusion into the SCS is enhanced which further modifies the upper and middle layer circulation of the SCS. The reduced planetary vorticity transport during El Niño results in a weakened cyclonic circulation and thinner mixed layer in the southern SCS. The modulations of the cyclonic circulation in the southern SCS, Vietnam offshore jet, and the coastal current during ENSO event enhance oceanic advection that favors an ocean-forcing energy exchange to the atmosphere across the air–sea interface. The relative importance of atmospheric and oceanic forcing on the SST change during the ENSO evolution is verified using a heat budget analysis for different regions of SCS. In the El Niño following spring, the advective term due to anomalous Ekman drift dominates the cooling process in the northern and eastern SCS. These thermal structure changes in the SCS are contributed by the wind–current–topography interactions.

1. Introduction

The South China Sea (SCS) is one of the world's largest marginal seas (Fig. 1). Its surface thermal conditions greatly affect the weather and climate conditions in the sea and its adjacent landmass. Particularly, the thermal conditions influence the path and intensity of tropical cyclones that travel across the SCS (Wang et al., 2007). Surface circulation in the SCS is mainly driven by seasonally reversed monsoon winds, which are southwesterly in summer and northeasterly in winter (Fang et al., 1998; Hu et al., 2000; Qu, 2000). Asian monsoons also control water exchange between the SCS and adjacent seas. For example, warm Indian Ocean surface water flows northward through the Karimata Strait into the SCS in summer. During winter, a branch of the warm Kuroshio Current flows into the northeastern SCS through the Luzon Strait (Qu et al., 2009; Fig. 1).

The connection between the SCS's climate and the Pacific El Niño-Southern Oscillation (ENSO) has drawn considerable attention. Wang et al. (2000) suggested that the key system connecting El Niño events and the East Asian climate is an anomalous atmospheric anticyclone located in the Philippine Sea. During El Niño, an anomalous cyclonic atmospheric circulation forms north of the equator as a Rossby wave response to heating anomalies in the central equatorial Pacific. The anomalous northerlies to the west of the Rossby gyre advect low-background moist enthalpy (defined as $C_pT + L_vq$, where C_p and L_v denote the specific heat at constant pressure and the latent heat of vaporization, respectively) southward, leading to anomalous subsidence, which further induces an anomalous low-level anticyclone over the Philippine Sea as a Rossby wave response (Wu et al., 2017a,b; Li et al., 2017). This Philippine Sea anticyclone (PSAC) is a typical ENSO phenomenon affecting the East Asian climate (Zhang et al., 1999; Wang et al., 2000; Wang and Zhang, 2002). Anticyclonic anomalies typically develop rapidly in the western North Pacific during late autumn and then strengthen to reach their mature phase in winter (December to February). The anomalous winds reverse during La Niña (Hoerling et al., 1997; Lau and Nath, 2009). The surface heat flux (SHF), sea surface temperature (SST), and surface circulation in the SCS all change in response to an anomalous low-level anticyclone or cyclone. Rainfall is also decreased (increased) in the SCS during El Niño (La Niña) (Chao et al., 1996; Wang et al., 2006; Yang et al., 2015; Chen et al., 2018). Satellite and in situ measurements have revealed substantial warming in the SCS during El Niño, and the role of ocean advection caused by the anomalous wind has been discovered to be crucial to the warming process (Wang et al., 2002; Xiao et al., 2018). Furthermore, a double peak in the SST evolution following El Niño events has been observed, with the maximums occurring in February and August (Wang et al., 2006; Liu et al., 2014).

* Corresponding author.
E-mail address: tsengyh@ntu.edu.tw (Y.-H. Tseng).

https://doi.org/10.1016/j.ocemod.2020.101655
Received 17 January 2020; Received in revised form 3 May 2020; Accepted 21 June 2020
Available online 25 June 2020

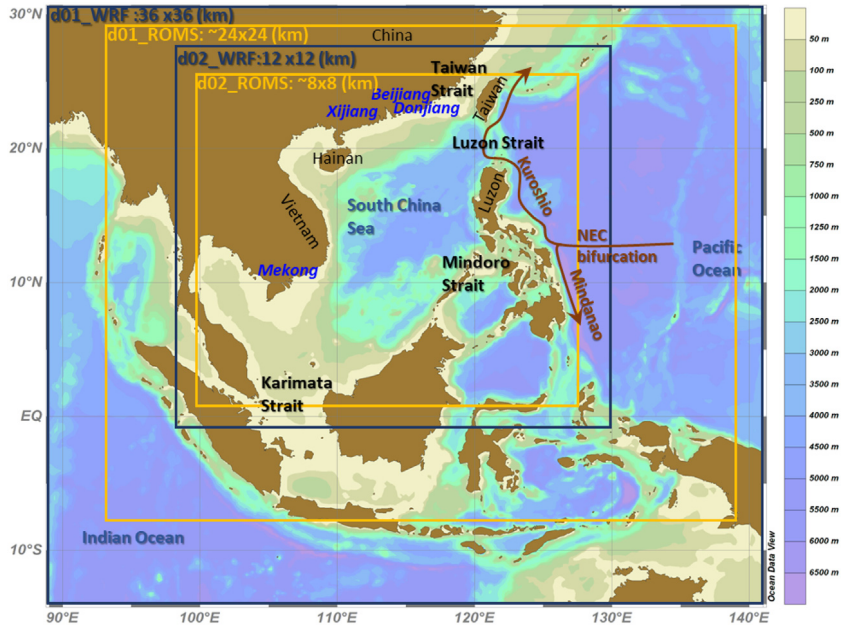

Fig. 1. The nested model domains and topography (shaded). Four major straits that connect the SCS to the open oceans are labeled in black. The major river discharges into the SCS are shown in blue.

Relevant studies have primarily used low-resolution atmospheric and satellite data to clarify the large-scale influence of the ENSO on the surface of the SCS. However, ocean mesoscale features may play a crucial role in the local air–sea process and provide feedback to the regional weather system (as well as global climate variability). Bishop et al. (2017) reported that in addition to atmospheric thermal forcing, eddy stirring in the ocean can strongly influence SHF variability. Qu et al. (2004) reported that in addition to anomalous low-level circulation triggering air–sea interactions in the SCS, horizontal heat transport through the Luzon Strait is a critical process that conveys the impact of the ENSO into the SCS. Many questions remain unanswered, such as how the surface and subsurface ocean circulations in the SCS change in response to the phases of the ENSO. The associated ocean processes and the roles of mesoscale oceanic features in the ENSO-related air–sea process also remain to be identified.

In this study, we employed a high-resolution coupled model to investigate the process associated with the ENSO's effect on the SCS. The coupled model reveals strong air–sea heat exchange anomalies and the relative contributions of the ocean and atmosphere in response to ENSO variability. To our knowledge, the ocean processes have not yet been examined carefully. Our results suggest the essential roles of mesoscale features in the regional air–sea interaction triggered by anomalous atmosphere circulation. To reduce the complexity resulting from the ENSO's decadal modulation (e.g., Hu et al., 2017), we select two strong events from the last decade: the 2015–2016 El Niño and 2011–2012 La Niña events. By comparing our results with the average of the atmosphere low-level circulation from six strong ENSO events (El Niño: 1997–1998, 2009–2010, and 2015–2016; La Niña: 1999–2000, 2007–2008, and 2011–2012) using the National Centers for Environmental Prediction (NCEP) reanalysis, we confirm that these two selected years are representative of PSAC variation over the SCS for the general ocean response during the ENSO decay of winter to spring regardless of the type of El Niño events. The central Pacific and eastern Pacific types of El Niño may cause some slightly different SST warming in the SCS, mostly resulting from the actual location of the anomalous low-level anticyclone (Liu et al., 2014), but do not affect the generality of the conclusion in this paper (see the Appendix for further discussion). Wang and Wang (2013) classified the central Pacific type of El Niño (El Niño Modoki) into two groups: El Niño Modoki I and II. Tan et al. (2016) suggested that the response of SST anomalies was similar during the canonical El Niño and El Niño Modoki I, whereas differences existed for El Niño Modoki II. The response of the SCS to Modoki II requires further investigation but is beyond the scope of this study.

Our major results address the following four aspects: anomalous atmospheric circulation over the SCS associated with the ENSO, the associated response at the SCS surface, local air–sea heat exchange, and the subsurface SCS response.

2. Model and observational data

2.1. Atmosphere–ocean coupled model

The Coupled Ocean–Atmosphere–Wave–Sediment Transport modeling system, developed at Woods Hole Coastal and Marine Science Center in the United States, has three state-of-the-art dynamic components for modeling the atmosphere, oceans, waves, and coastal environments (Warner et al., 2010); these components are the Weather Research and Forecasting (WRF) model (Skamarock et al., 2005), regional ocean modeling system (ROMS), and simulating waves nearshore model. These individual models communicate through the model coupling toolkit using the message passing interface to exchange model state variables (Warner et al., 2010). To emphasize the interaction between the ocean and atmosphere in this study, we only couple the ocean and atmosphere components without considering wave effects. A pair of two-way nested domains is used for both atmosphere and ocean models (Fig. 1). The horizontal resolution for the first (outer) domains is 36 and 24 km for the WRF model and ROMS, respectively, whereas that of the second (inner) domains is 12 and 8 km (1/3 of the first domain). Vertically, 36 and 25 levels are used in WRF model and ROMS, respectively. The NCEP Final (FNL) Operational Model Global Tropospheric Analyses data are used as the initial and lateral boundary conditions (updated every 6 h) for the WRF model. The ROMS uses realistic topography from the ETOPO2 (US Department of Commerce, National Oceanic and Atmospheric Administration, National Geophysical Data Center, 2006). The global 1/12° ocean predictions with the Hybrid Coordinate Ocean Model or Navy Coupled Ocean Data Assimilation Analysis data are used as the initial and lateral boundary conditions (updated every 10 days). The El Niño simulation period is November 1, 2015 to June 30, 2016, and the La Niña simulation period is November 1, 2011 to June 30,

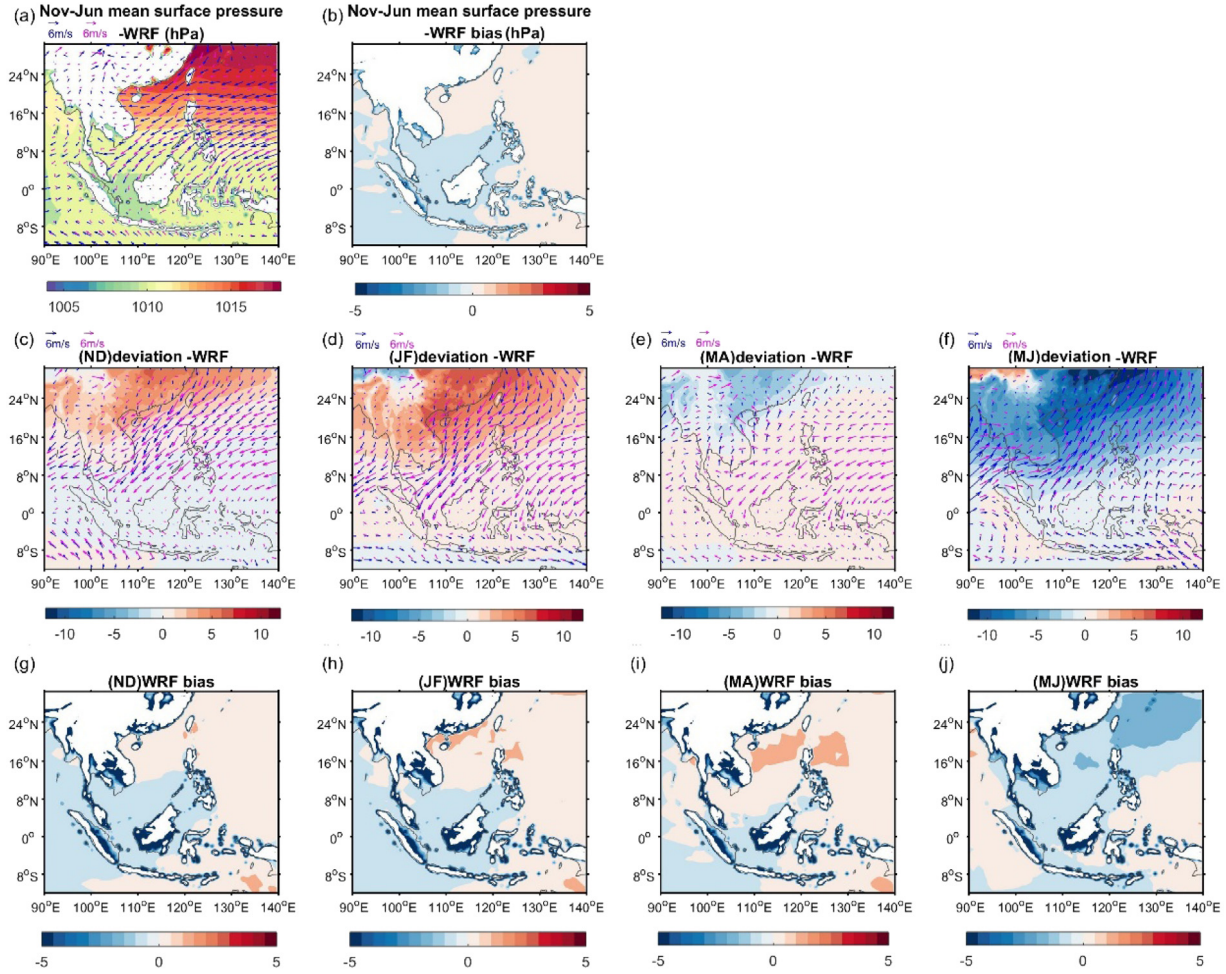

Fig. 2. (a) The modeled 8-month averaged (2015/11–2016/6) SLP (hPa, shaded) and surface wind vectors (magenta vectors) superimposed by the NCEP Reanalysis wind (blue vectors). (b) SLP biases (model-reanalysis, hPa).(c)–(f) 2-month averaged (Nov–Dec, Jan–Feb, Mar–Apr, May–Jun) SLP and surface wind vectors (magenta vectors: model, blue vectors: reanalysis) deviated from the average shown in (a). (g)–(j) 2-month averaged SLP biases (hPa).

2012. The major river runoffs included in the ROMS (marked in Fig. 1) are based on the climatological monthly river runoff data retrieved from the Global River Flow and Continental Discharge Dataset [(http://www.cgd.ucar.edu/cas/catalog/surface/dai-runoff/); see Dai (2016) for a detailed description]. Note that Xijiang, Beijiang, and Dongjiang all contribute to the Pearl River estuary.

2.2. Observational and reanalysis data

Moderate Resolution Imaging Spectroradiometer (MODIS) level 3 monthly SST images (http://dx.doi.org/10.5067/MODST-MO4D4) are used to examine the SST patterns during the two ENSO decaying years. The ground resolution of the MODIS is approximately 4 km. In addition, temperature–salinity (T–S) profiles provided by the global array of Argo floats are used for the validation (freely available from http://www.argo.ucsd.edu and http://argo.jcommops.org).

The monthly mean sea level pressure (SLP) and surface wind data from the NCEP reanalysis (http://www.esrl.noaa.gov/psd/data/gridded/data.ncep.reanalysis.derived.html) were also compared with the low-level atmospheric circulation in the model results. The ocean reanalysis, HYCOM GOFS 3.1 Global Ocean Forecasting System (HYCOM + NCODA Global 1/12° Analysis), is retrieved from http://tds.hycom.org/thredds/catalogs/GLBv0.08/expt_53.X.html. Data after 2015 is retrieved from http://tds.hycom.org/thredds/catalogs/GLBv0.08/expt_56.3.html. The temporal and spatial resolutions of GOFS 3.1 are 3-h and 0.08°, respectively.

3. Results

3.1. Model validation: seasonal variation in the SCS

Fig. 2a plots the modeled 8-month-averaged (November 2015 to June 2016) pattern of low-level circulation. The modeled biases (model-reanalysis) are shown in Fig. 2b. The average model circulation pattern is similar to the NCEP reanalysis, showing prevailing northeasterly winds in the SCS. Fig. 2c–f shows that the consecutive 2-month-averaged patterns deviate from the 8-month-averaged pattern in Fig. 2a. The biases of the 2-month-averaged patterns are shown in Fig. 2g–j. During the early winter (November–December), northeasterly wind anomalies prevail in the SCS with positive SLP anomalies centered in China. The anomalies continually strengthen during January–February and later change to negative and positive SLP anomalies in China and the central SCS, respectively. Southerlies dominate the low-level winds in the SCS during May–June. The modeled seasonal variation and patterns are generally consistent with the reanalysis.

Fig. 3a, b present a comparison of the 8-month-averaged SST patterns between the model results and MODIS SSTs for the same time period. The modeled pattern is in favorable agreement with the observed MODIS SSTs with slightly lower SSTs in the model. The average SST decreases gradually from the southeast of the SCS to the northwest. The coolest temperature is observed off the continental shelf of the SCS, and the Kuroshio intrusion into the SCS results in a warm tongue in the Luzon Strait (Fig. 3a, b). The consecutive 2-month-averaged

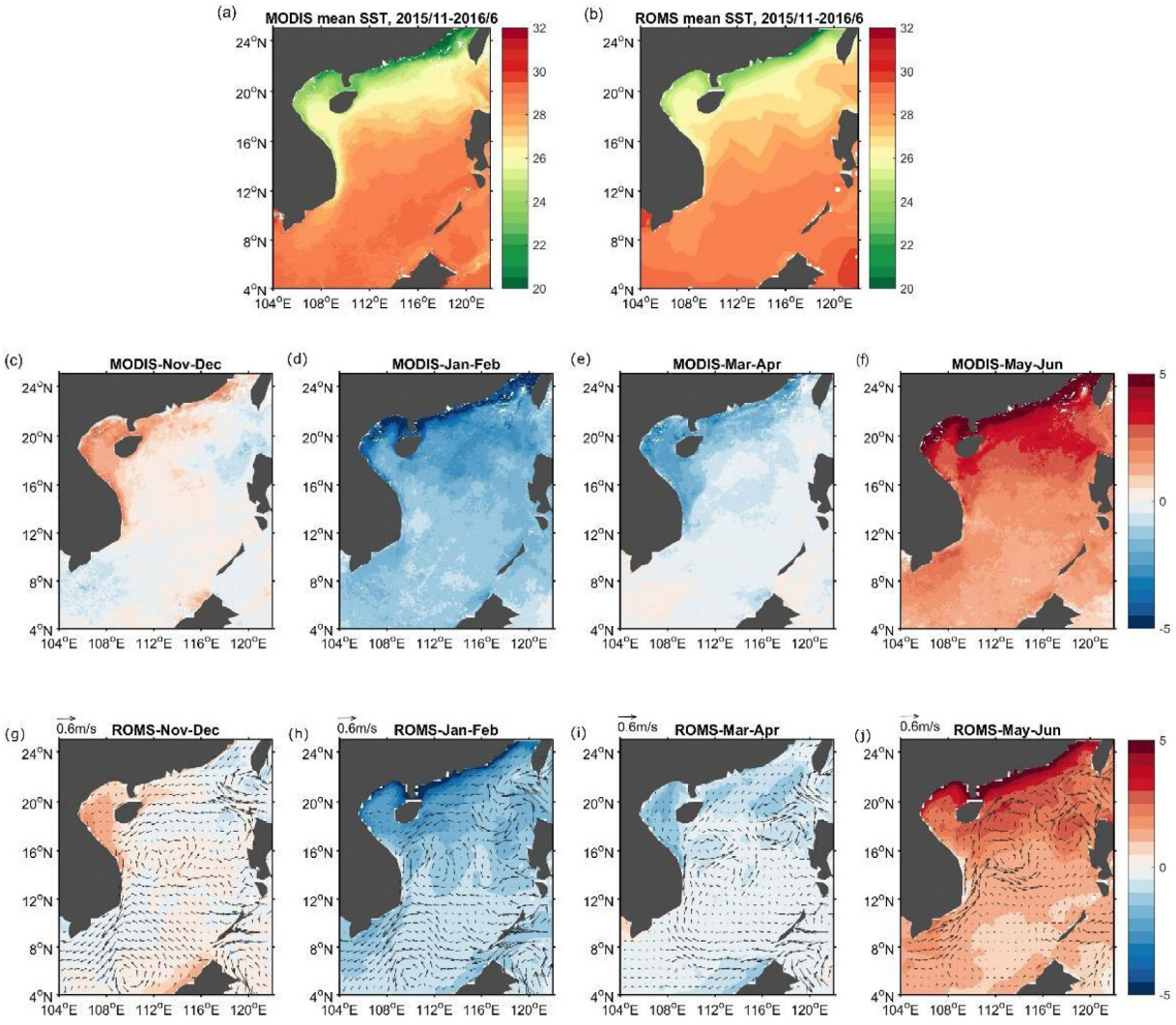

Fig. 3. The 8-month averaged (2015/11–2016/6) SST (°C) from (a) MODIS and (b) model results. (c)–(f) 2-month averaged (Nov–Dec, Jan–Feb, Mar–Apr, May–Jun) of the MODIS SST deviated from the average shown in (a). (g)–(j) 2-month averaged of the model SST deviation from the average shown in (b). The averaged surface currents are superimposed as vectors.

patterns (Fig. 3c–j) deviate from the average fields presented in Fig. 3a and b. Both the observations and the model reveal that the coolest SSTs occur during January–February, with the SSTs then gradually increasing throughout May–June; this warming occurs more quickly in the northern SCS than the other regions. The fastest warming occurs along the coast of southern China because of this coast's extremely shallow shelf. The modeled ocean surface currents (2-month-averaged vectors are superimposed on the bottom panels in Fig. 3) also indicate a southward western boundary current in the SCS, resulting in a cyclonic circulation in the southern SCS during the northeasterly winter monsoon (November–February). In addition, the Kuroshio intrusion into the SCS through the Luzon Strait is considerable. These surface current features are consistent with those reported previously (Hu et al., 2000).

Additional comparison of the modeled subsurface T–S data with the available Argo floats is provided in Fig. 4. To quantitatively compare the T–S data, we defined three regions from north to south, namely west of the Luzon Strait (R1), west of Luzon Island (R2), and east of Vietnam (R3); the regions are indicated in Fig. 4a (all available trajectories from January to June 2016 are shown). The 2-month-averaged T–S data (lines in Fig. 4b–g) in these regions are directly compared with the Argo data (dots) for the upper 500 m. In R1 and R2, the modeled temperature and salinity profiles are all within the observational range. In R3, the modeled surface salinity is slightly higher than the observation but is still within the range of the Argo data. At the subsurface, the modeled salinity profile values were lower than the observed values. Because Argo data are only available for May–June 2016 in R3 with relatively few Argo float sampling data, the available Argo data may not be representative for the 2-month average. The difference may also result from the direct impact of interannual varying freshwater Mekong River input (the climatological value is specified in the model). Additional simulation without the river runoff input in the model confirmed the key role of river runoff in the SCS salinity simulation. Without the river runoff data, the modeled surface salinity is completely outside the observational data (figure not shown). In general, the overall T–S characteristics in the SCS were reasonably represented by the model. Reasonable agreement with the observation in the La Niña year was also discovered (figures not shown).

3.2. Anomalous low-level atmospheric circulation associated with the ENSO

Fig. 5a–d displays the modeled 2-month-averaged SLP and surface wind differences between El Niño (2015–2016) and La Niña (2011–2012) (difference = El Niño value - La Niña value). Similar differences obtained from the NCEP reanalysis are superimposed (blue contours and vectors). The anticyclone in the central SCS appears in November–December. It intensifies during the matured ENSO (January–February) and then decays during the following months. In late spring (May–June), the anticyclone intensifies again, but its central location moves

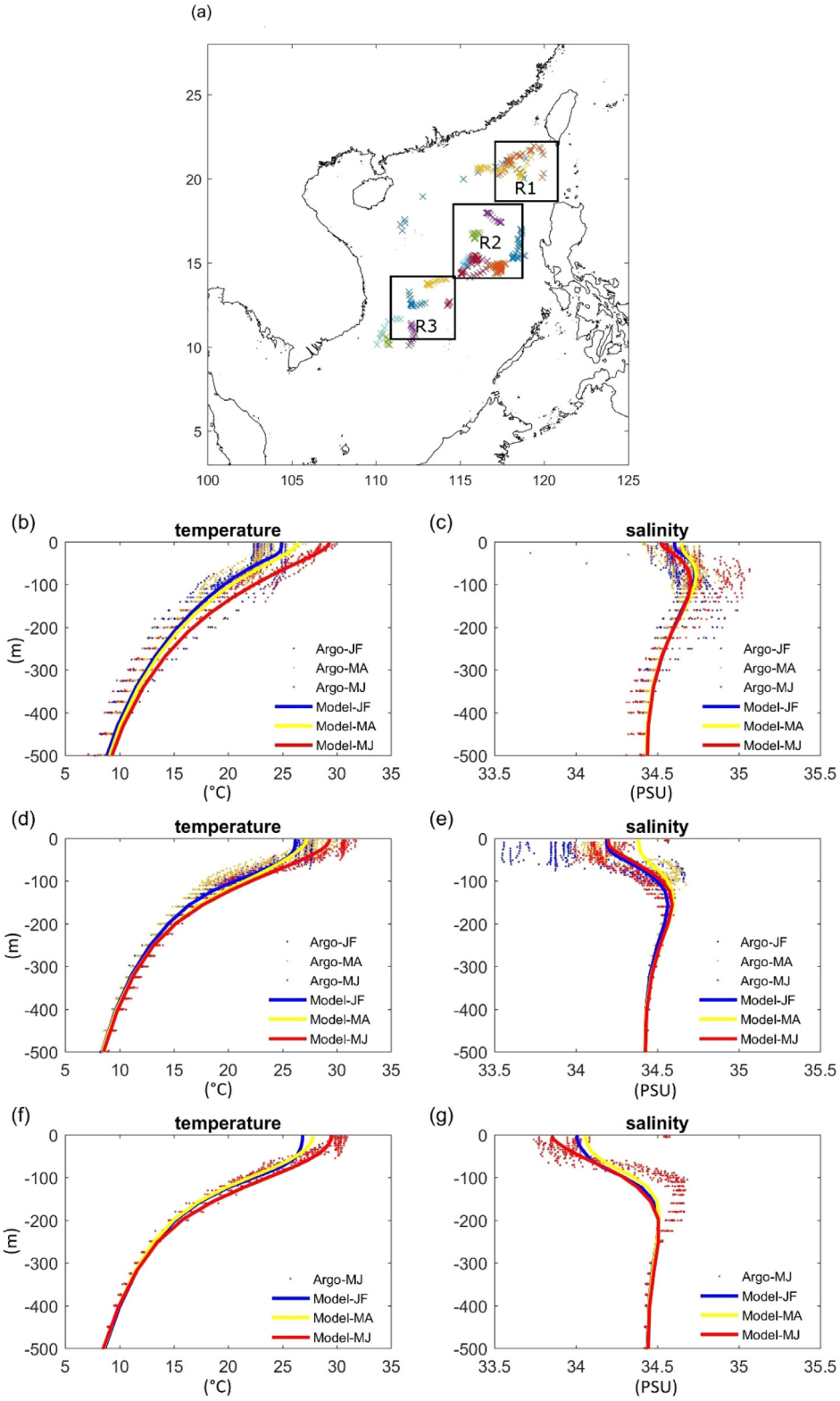

Fig. 4. (a) Available trajectories of the Argo floats between 2016/1 and 2016/6. Color indicates different floats, (b)–(c) the temperature and salinity profiles averaged over region R1 as shown in (a) from the Argo floats and the model results. (d)–(e) are the same as (b)–(c) but for region R2. (f)–(g) are the same as (b)–(c) but for region R3. In the R3 region, only the Argo data during May–Jun is available.

to the northern SCS, and this is accompanied by an enhanced easterly in the southern SCS. These features are similar to the NCEP reanalysis (Fig. 5e–h). The anomalous anticyclone-associated southwesterly/northeasterly in the northern/southern SCS indicates a weaker or stronger East Asian winter monsoon in different parts of the SCS during El Niño. The modeled anticyclonic circulation is stronger than the NCEP reanalysis, possibly due to the much finer resolution (24 km) in the current model. We note that the modeled location of the anomalous anticyclone slightly shifts westward compared to the NCEP reanalysis. This minor varying of location does not influence the major ocean

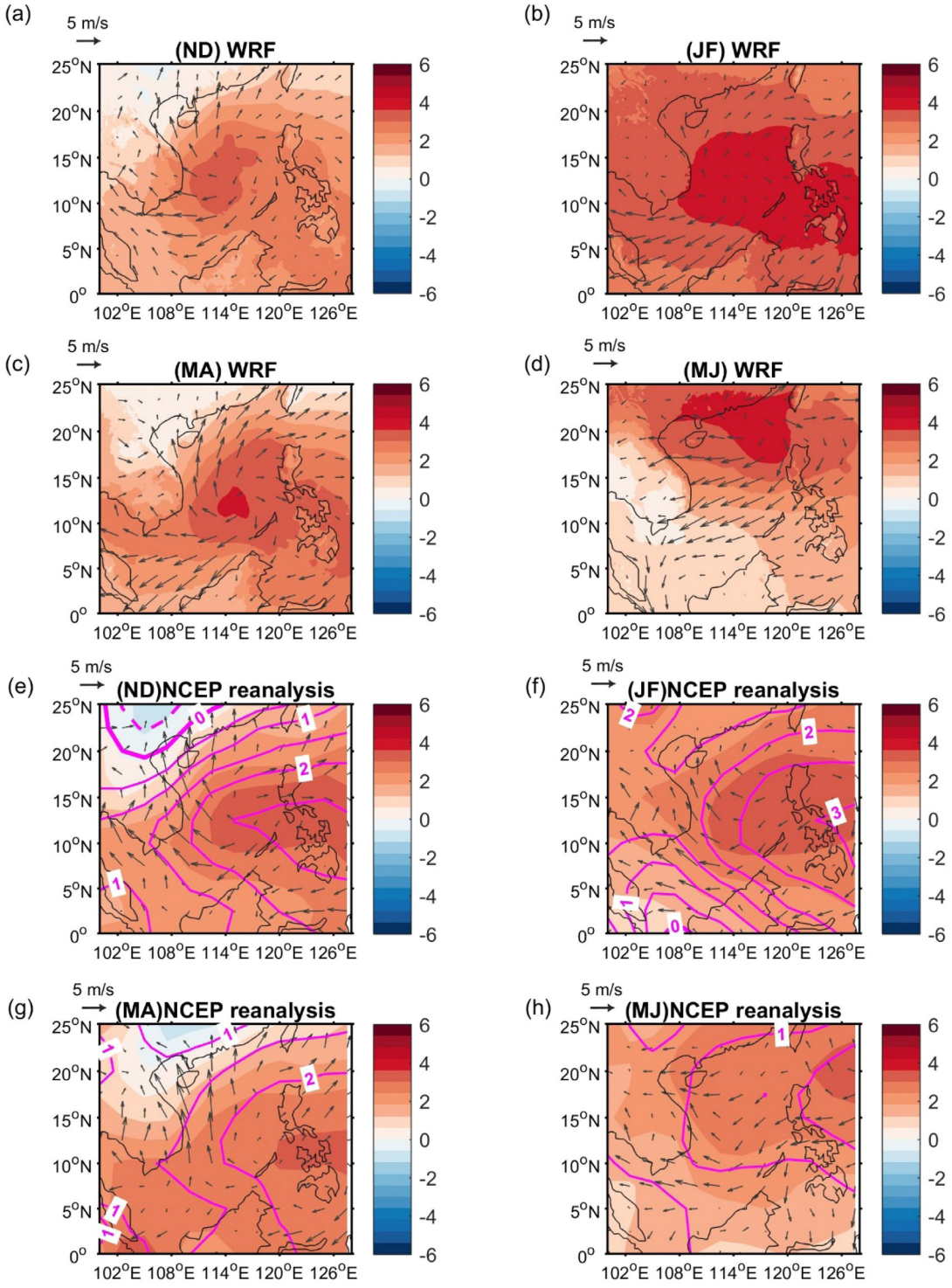

Fig. 5. The modeled 2-month averaged differences in the SLP (hpa, shaded) and surface winds (vectors) between El Niño and La Niña (former minus latter). (a) Nov–Dec, (b) Jan–Feb, (c) Mar–Apr and (d) May–Jun. Similar differences from the NCEP reanalysis are shown in (e)–(h). The averaged SLP differences in the six most recent ENSO events are shown as magenta contours.

responses discussed in the following sections since the anti-cyclonic (cyclonic) circulation is a very robust atmospheric feature during El Niño (La Niña) regardless of the strengths and types of ENSO events (Wang et al., 2000; Li et al., 2017; Wu et al., 2017a; Miller et al., 2017). Therefore, the important oceanic responses will not matter too much. We also perform additional ocean-only numerical experiments forced by the reanalysis to confirm this similarity (see the detailed comparison in the Appendix). The use of coupled model run here is to highlight not only the oceanic response but also the relevant air–sea interaction.

To confirm that the selected two years are representative of the general ENSO response, we superimposed the average SLP differences (magenta contours in Fig. 5e–h) from the six ENSO events (El Niño: 1997–1998, 2009–2010, and 2015–2016; La Niña: 1999–2000, 2007–2008, and 2011–2012; http://ggweather.com/enso/oni.htm). Similar patterns of SLP differences suggest that the anticyclone strengthens during January–February and then decays after March–April. This anomalous anticyclone forms because of the remote large scale ENSO impact (e.g., Wang et al., 2000; Wang and Zhang, 2002). We further discuss the

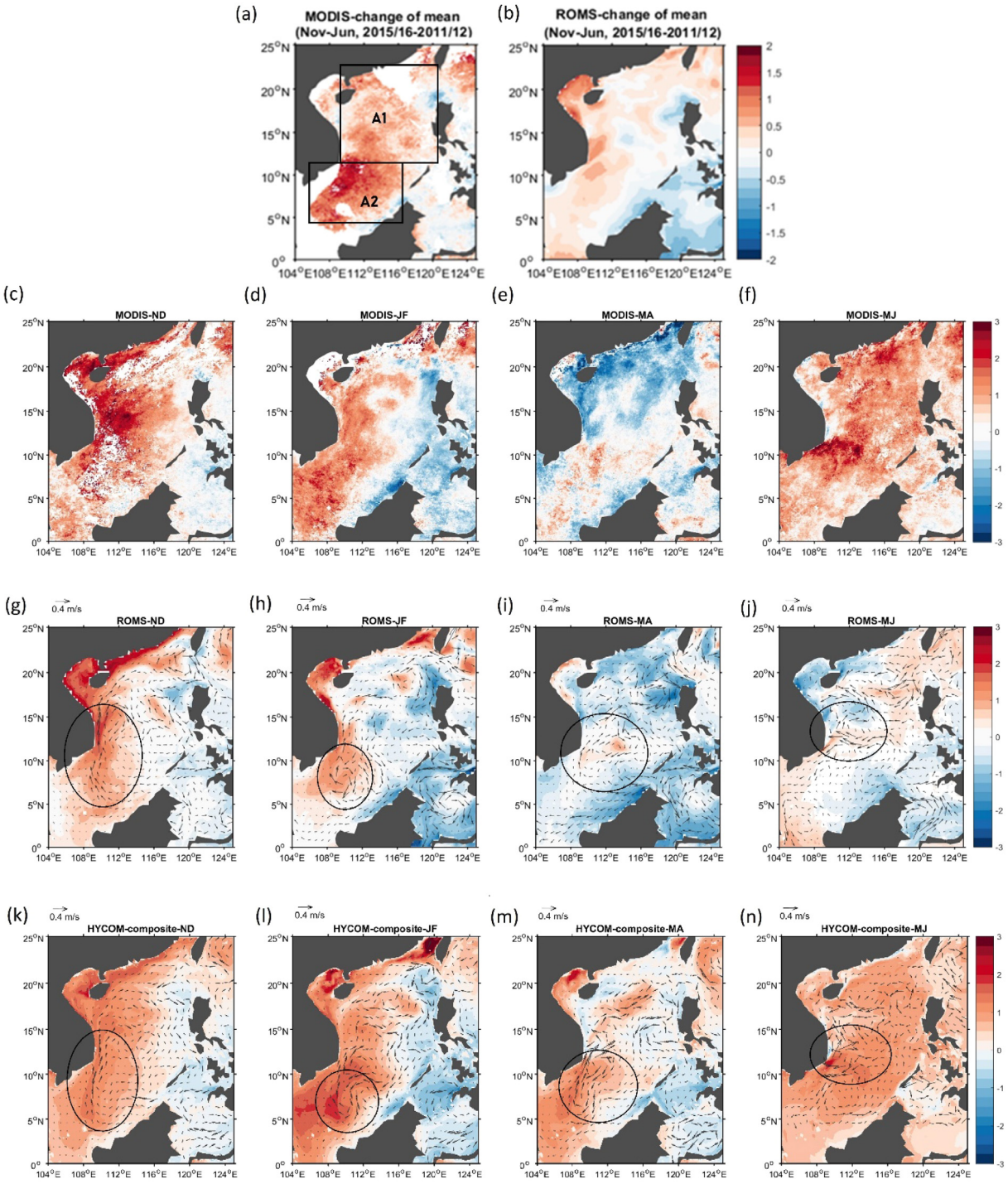

Fig. 6. 8-month averaged (Nov to Jun) SST (°C) differences between El Niño and La Niña from the (a) MODIS and (b) model results. (c)–(f) 2-month averaged (Nov–Dec, Jan–Feb, Mar–Apr, May–Jun) of the MODIS SST differences between El Niño and La Niña. (g)–(j) are the same as (c)–(f) but for the model SST and surface current difference. (k)–(n) the composite of 2-month mean differences in SST and surface current between positive and negative ENSO phases using HYCOM reanalysis (GOFS 3.1). El Niño: 1997/98, 2002/03, 2009/10, 2015/16; La Niña: 1999/00, 2007/08, 2010/11, 2011/12. The similar mesoscale features, such as western boundary current changes, the anticyclonic circulation in the southern SCS and the northward shift of the offshore jet off Vietnam, are marked by the black circles.

ocean's response to the anomalous low-level circulation and its coupled air–sea interaction in the following sections.

3.3. SCS ocean surface temperature and current response to the ENSO

Fig. 6a–b shows the November–June-averaged SST differences between the El Niño year and the La Niña year from the MODIS and the model. The general patterns are similar, but a weaker SST contrast was observed in the model than in the MODIS. This may be due to the higher skin temperature in the MODIS data than in the model's upper layer, which is assumed to be well mixed. The SST differences highlight the opposite dynamical processes in response to El Niño and La Niña, mostly positive to the east of Vietnam.

To further examine the seasonal evolution, consecutive 2-month-averaged differences in SST and model ocean surface flow between El Niño and La Niña are illustrated in Fig. 6c–j. The evolution (November

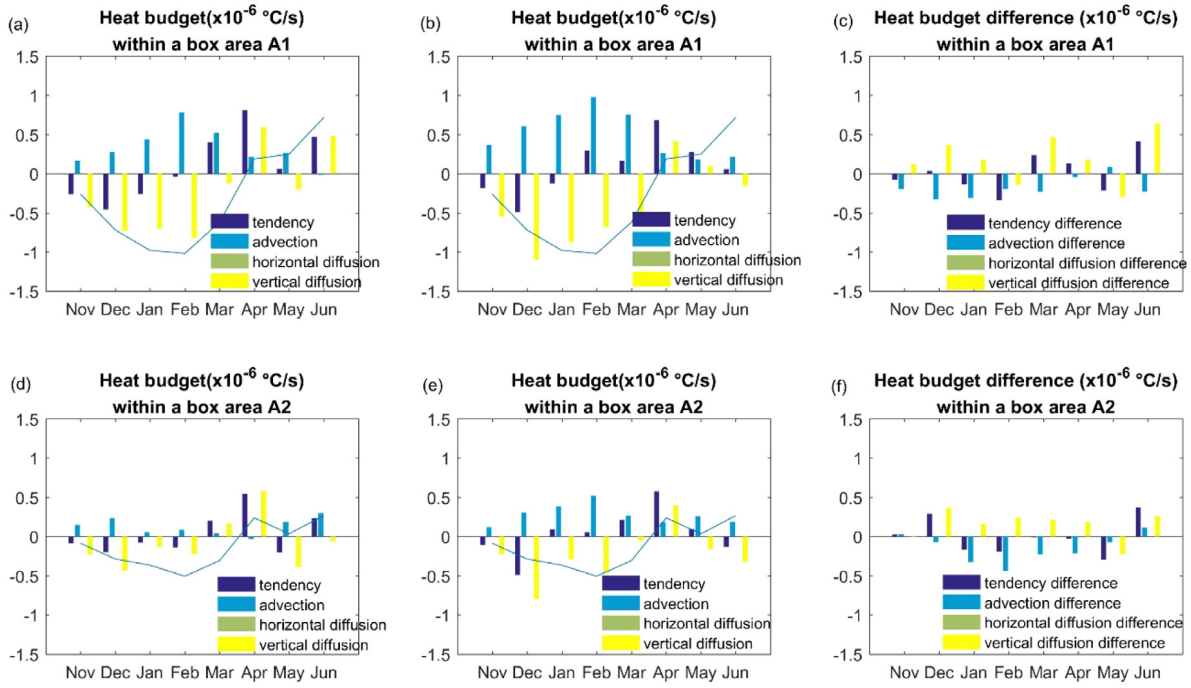

Fig. 7. Monthly heat budget (°C/s) in the surface layer averaged over A1 box (Fig. 6a) during (a) El Niño, (b) La Niña, (c) their difference (El Niño- La Niña). (d)–(f) are for A2 box. Blue lines are the accumulation of the monthly tendency terms.

to June) in SST difference is similar to that in the MODIS data except that the simulated warming during January–February is weaker than the observation and the model indicates slower warming from March–April to May–June. During November–February (northeasterly monsoon), the anomalous low-level anticyclonic circulation weakens the northeasterlies over the northwestern SCS. In the ocean, the surface current difference off the Vietnam coast is northward (Fig. 6g–i), suggesting a weak western boundary current during El Niño. This phenomenon has been confirmed using long-term altimetry and in situ data (Zu et al., 2019). The surface current difference also reveals an anticyclonic mesoscale feature in the southern SCS, weakening the existing cyclonic eddy in the same location during El Niño (Fig. 3g–h). West of the Luzon Strait, the anticyclonic feature suggests the enhancement of Kuroshio intrusion during El Niño, whereas the Kuroshio loop is common in winter.

We next examine the evolution of SST differences. In November and December, positive SST differences occur in the western SCS (Fig. 6g). The amount of advective cool water is reduced because of the weakened southward boundary current during El Niño. This effect together with reduced upward surface turbulent heat flux in the northwestern SCS during an El Niño winter leads to relatively large positive SST anomalies in the western SCS (heat budget and air–sea heat exchange is discussed in the following sections). In January–February, the positive SST differences in the western SCS are decreased. During March–April, the northerlies weaken and are gradually replaced by southerlies, leading to a northward western boundary current (Fig. 3i). The SST differences mostly become negative in the northern SCS during this period. Simultaneously, an anticyclonic feature forms to the west of the Luzon island during El Niño, lasting through early summer. This feature was noted and explained by Chu and Chang (1997).

During the subsequent May–June, a positive SST occurs again over the eastern SCS and northwestern Pacific region. This rewarming phenomenon after El Niño was reported by Xie et al. (2009), who suggested that the SST increase during the summer of an El Niño decaying year is due to enhanced high pressure resulting from the equatorial Kelvin wave triggered by tropical Indian Ocean warming. During May–June, a pair of cyclonic–anticyclonic features exists to the east of Vietnam (10°–15°N). These features suggest a northward shift of the offshore jet to the east of Vietnam during spring to early summer. The meridional displacement of the jet associated with the ENSO has been observed using satellite data (Li et al., 2014); it was due to the anomalous and simultaneous easterly wind in the central SCS (Fig. 5).

To further confirm the chosen ENSO years reflect the general responses to ENSO, we calculate the same upper ocean responses using the composite of HYCOM reanalysis from the 8 strongest ENSO cases in the recent decades (Fig. 6k–n); El Niño: 1997/98, 2002/03, 2009/10, 2015/16; La Niña: 1999/00, 2007/08, 2010/11, 2011/12. The composite shows similar SST and surface current difference (marked by black circles in Fig. 6), except positive SST difference during March–April (negative in the difference between 2015/16 and 2011/12). However, the overall SST tendency from winter to spring and early summer is similar to the chosen ENSO years.

3.3.1. Heat budget analysis

Fig. 6 suggests that the SST in the SCS responds differently during differing ENSO decay phases. Negative tendency is found in the SST difference from November–December to March–April, with the largest change in the northern SCS. We quantify the associated physical processes using monthly heat budget analysis (Eq. (1)).

$$\frac{\partial T}{\partial t} + u\frac{\partial T}{\partial x} + v\frac{\partial T}{\partial y} + w\frac{\partial T}{\partial z} + \frac{\partial}{\partial z}\left(k\frac{\partial T}{\partial z}\right) + \nabla A_h \nabla T = 0 \quad (1)$$

The first term is the surface layer temperature tendency, followed by the advection term associated with horizontal and vertical fluid motions. The last two terms are vertical and horizontal diffusion. The vertical diffusion term is represented by the difference between the net SHF and turbulent flux at the bottom of the ocean surface layer (positive downward, i.e., warming the ocean). The horizontal diffusion is negligible. Fig. 7 presents the surface layer heat budgets averaged over two boxes (northern SCS: A1; southern SCS: A2; illustrated in Fig. 6a) for El Niño (left), La Niña (middle) and their differences (right). The accumulated monthly tendency term is superimposed as a blue line and reflects the temperature change from the initial condition. We note that the November initial SST for the El Niño (2015–2016) simulation is higher than that for the La Niña (2011–2012).

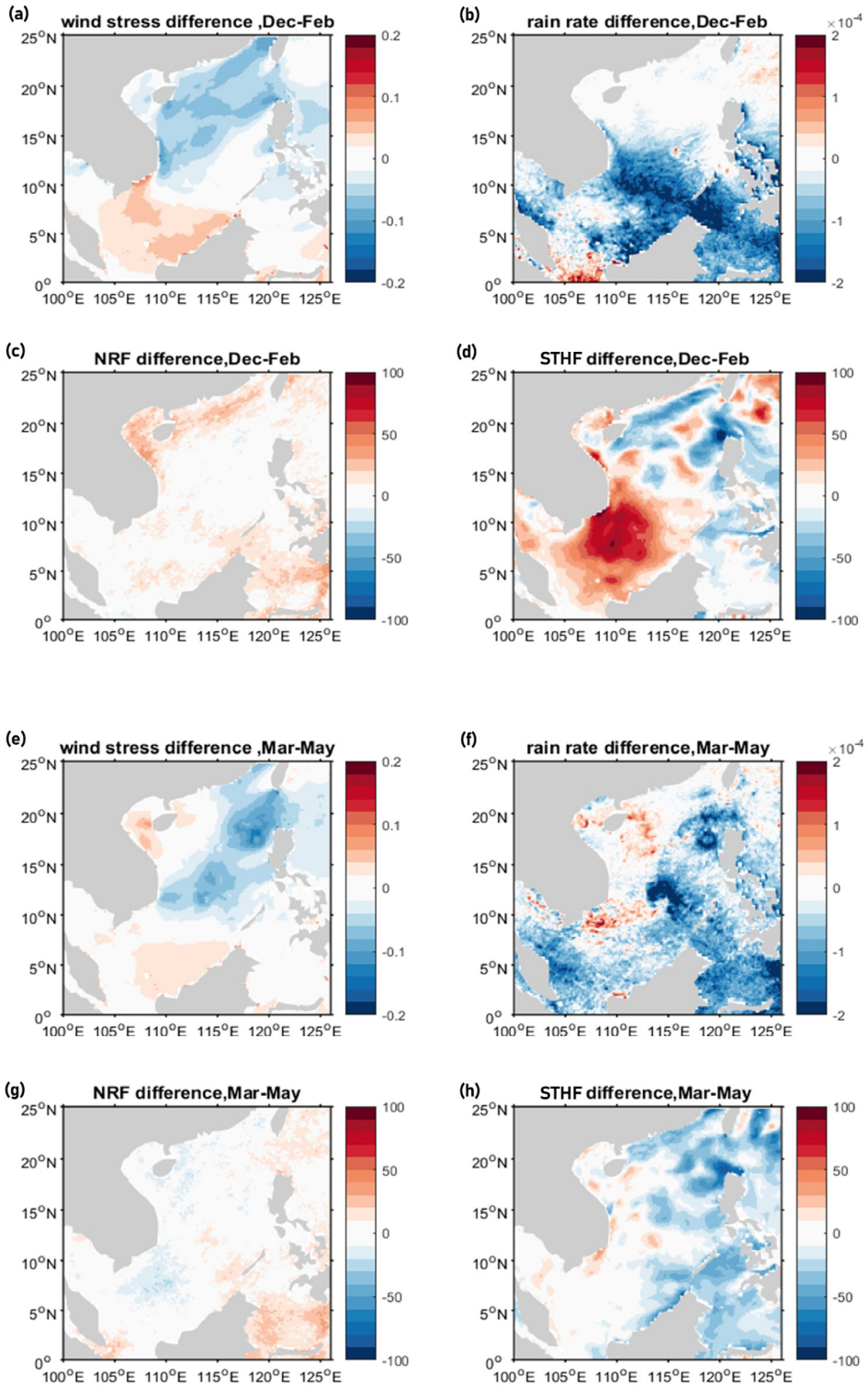

Fig. 8. The mean difference in the (a) wind stress (N/m^2), (b) rain rate (kg/s m^2), (c) net radiative flux (watt/m^2), and (d) surface turbulent heat flux (watt/m^2, latent heat flux + sensible heat flux) between the El Niño and La Niña (former minus latter) during winter (Dec–Feb). (e)–(h) the same as (a)–(d) except during spring (Mar–May). Positive is upward in difference.

In the northern SCS (A1 region; Fig. 7a–c), during winter, the surface layer is cooled in both El Niño and La Niña, resulting mainly from the vertical diffusion term (Fig. 7a–b). During spring, the vertical diffusion becomes positive (warming) and the advective warming is as important as the warming by the vertical diffusion. During winter to spring, the diffusion term (advection term) in El Niño is weaker (stronger) than in La Niña (Fig. 7c). This is mainly due to the presence of anomalous anticyclonic circulation in the low-level atmosphere that suppresses the upward SHF by reducing surface wind speed. The advection term plays a crucial role in bringing warm water northward to the northern SCS to compensate for heat loss. The difference in the advection term can also be viewed as an anomalous Ekman drift

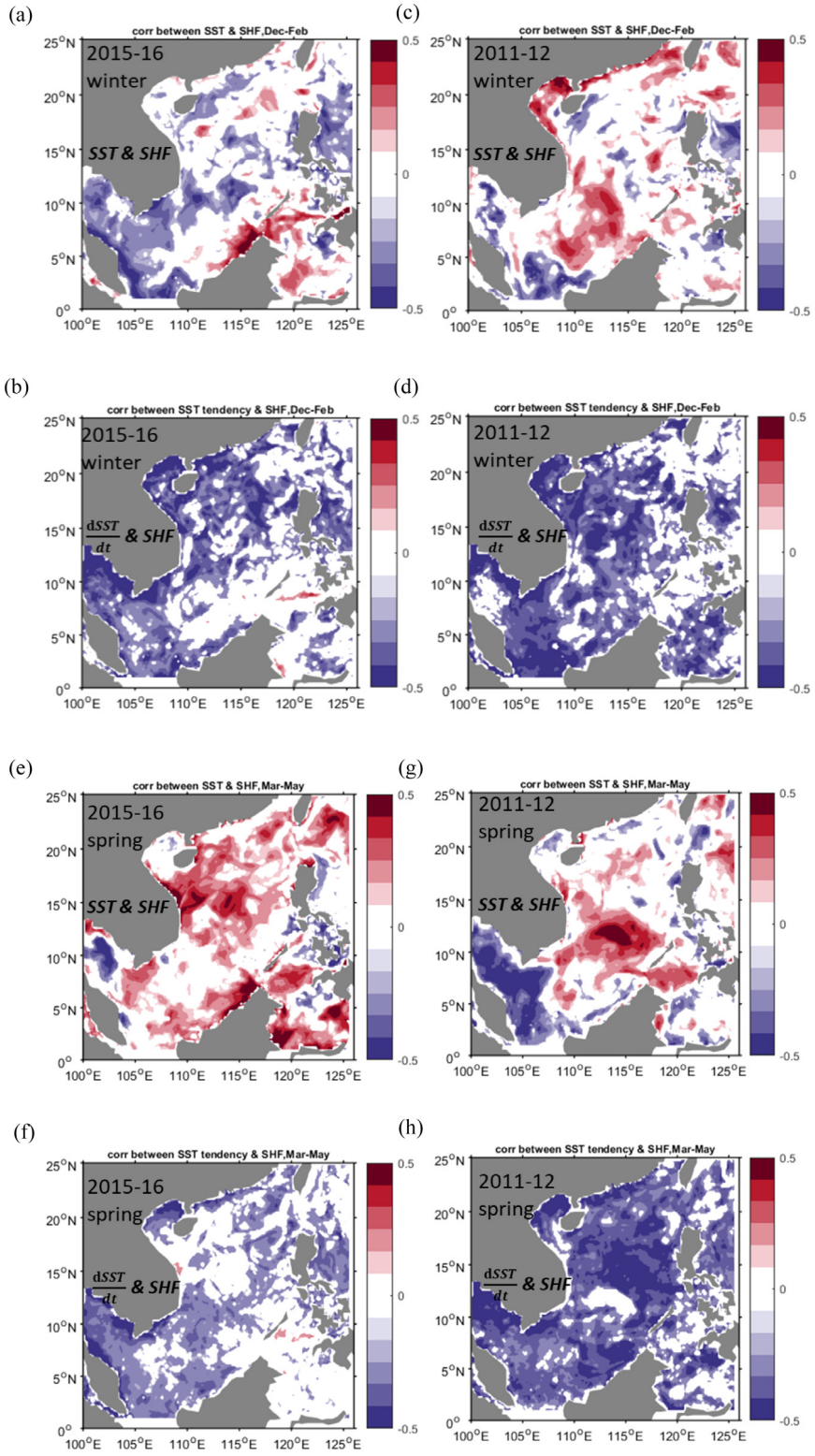

Fig. 9. Relationship between the SST/SST tendency and SHF anomalies during winter (Dec–Feb). (a)–(b) El Niño and (c)–(d) La Niña. (e)–(h) the same as (a)–(d) except during spring (Mar–May). The anomalies are calculated by subtracting the climatological monthly mean of NCEP reanalysis (1979–2009). Only values above 90% significance level are shown.

toward southeast in the northern SCS during El Niño, triggered by the southwesterly anomalies. This transport results in the spread of cooler water in the coastal region of the northwestern SCS toward the eastern SCS. Our budget analysis suggests that in the northern SCS (A1 box), weaker upward SHF during El Niño winter causes higher surface temperature than the La Niña winter, whereas lower ocean advection during the El Niño spring causes lower surface temperature than the La Niña spring.

In the southern SCS (A2 box; Fig. 7d–f), the SST is higher and more homogeneous than that in the northern SCS (Fig. 3a–b). Comparing the

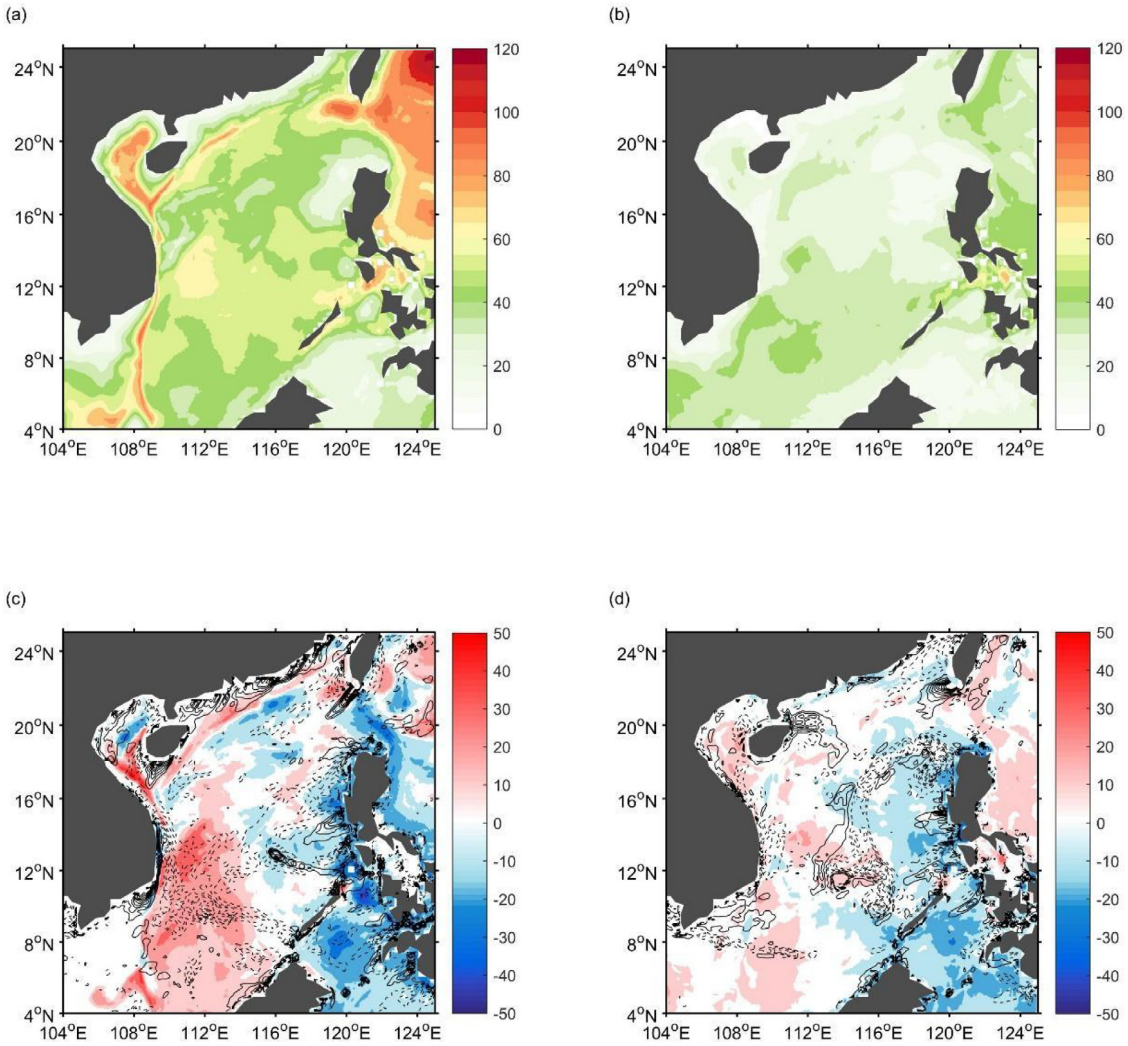

Fig. 10. (a) Winter (Dec–Feb) and (b) spring (Mar–May) MLD (m) in the El Niño. The corresponding MLD differences between El Niño and La Niña (former minus latter) are shown in (c) winter and (d) spring. The surface wind stress curl differences are shown as black (contour interval 3×10^{-7} Nm^{-3}). Negative wind stress curl is dashed.

two ENSO events, both the advection and vertical diffusion terms are larger during La Niña. The advection is crucial for warming during La Niña winter. This is associated with a stronger cyclonic circulation in the southern SCS. During El Niño spring, the temperature tendency is mainly determined by the vertical diffusion term. However, during La Niña spring, it is determined by both advection and vertical diffusion.

3.3.2. Air–sea heat exchange

Fig. 8 illustrates the mean differences in wind stress, rainfall rate, net radiative flux, and surface turbulent heat flux (STHF = latent heat flux + sensible heat flux) between El Niño and La Niña (difference = El Niño value - La Niña value) during the winter (December–February) and spring (March–May). A positive heat flux difference indicates an upward difference (i.e., more flux released to the atmosphere during El Niño than La Niña). The lower rain rate in the El Niño winter is mainly due to the anomalous descending flow under the anomalous anticyclonic circulation in the low-level atmosphere (Fig. 8b). The net radiation flux differences (Fig. 8c) are relatively small compared with the STHF differences (Fig. 8d). Regarding the wind stress and STHF differences, we can clearly observe opposite features between the northern and southern SCS, mainly due to the anomalous low-level anticyclonic circulation (Fig. 5) that reduces (enhances) the wind speed in the northern (southern) SCS during El Niño. In addition, the higher SST in the southern SCS during El Niño contributes to the larger STHF than during La Niña (Fig. 6). Note that in the heat budget, the vertical diffusion term is weaker in El Niño than La Niña (Fig. 7d–f), even with a stronger surface heat flux in the southern SCS (Fig. 8d). This is because during La Niña, the cyclonic circulation in the southern SCS is stronger accompanying with a thinner mixed layer depths (MLDs) (Figs. 3g–i and 6g–h) that enhances turbulent flux at the bottom of the surface layer.

Similar contrast patterns can be observed in the wind stress, rain rate, net radiative flux, and STHF in the northern SCS during spring (Fig. 8e–h). In the southern SCS, the large STHF pattern during the winter is absent during spring, because the SST contrast quickly decreases over time (Fig. 6).

To further investigate the relative contribution of the ocean and the atmosphere in the heat flux variations associated with ENSO variability, we evaluated the relationship between the SST, SST tendency (rate of SST change), and SHF across the ocean surface, which can help us identify whether the ocean drives atmospheric SHF variability or the atmosphere forces ocean SST variability (Wu et al., 2006; He and Wu, 2013). The statistical relationship has been clarified using simple stochastic models (von Storch, 2000; Wu et al., 2006). The local energy balance of the coupled atmospheric system is as follows:

$$\frac{dT_a}{dt} = \alpha(T_o - T_a) - \gamma_a T_a + N_a$$
$$\frac{dT_o}{dt} = \beta(T_a - T_o) - \gamma_o T_o + N_o$$

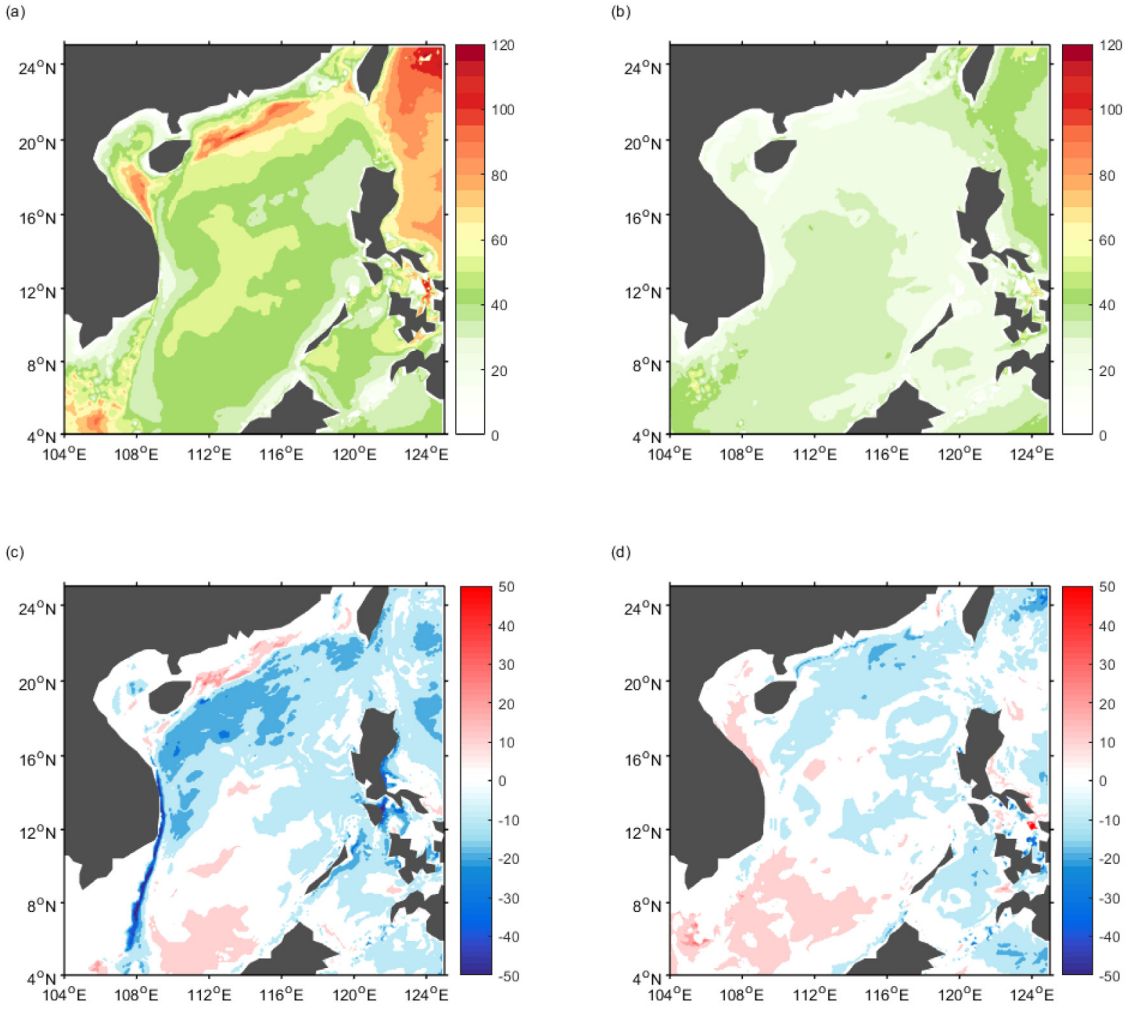

Fig. 11. Composite of MLDs during El Niño (a) Winter (Dec–Feb) and (b) spring (Mar–May) using the HYCOM reanalysis (GOFS 3.1). The composite of MLD differences between El Niño and La Niña during (c) winter and (d) spring. (El Niño: 1997/98, 2002/03, 2009/10, 2015/16; La Niña: 1999/00, 2007/08, 2010/11, 2011/12).

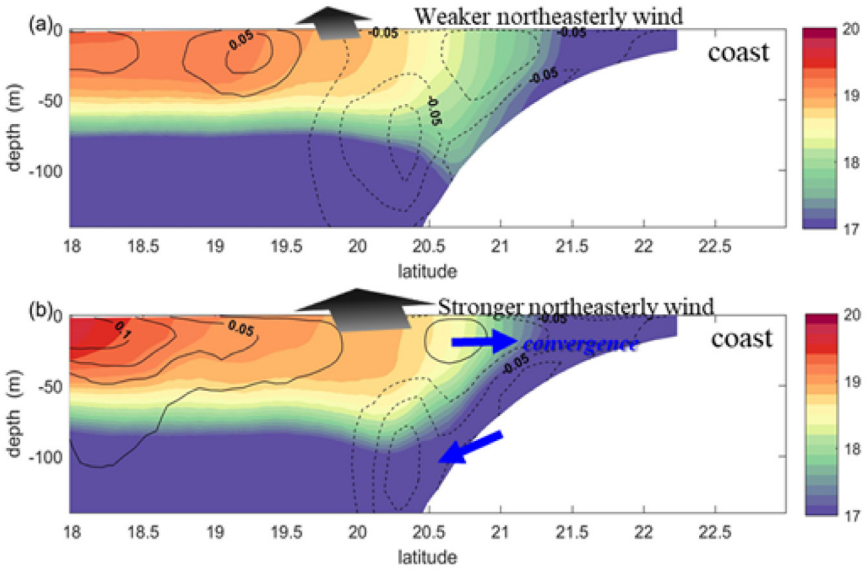

Fig. 12. Time-averaged temperature (°C, shaded) and v-velocity (m/s, contours) along 114°E, 18-23°N during El Niño and La Niña, respectively. The schematic arrows show the formation of a thicker MLD during El Niño year in the shelf break (20.5–21.5°N) result mainly from heat flux diffusion term.

Table 1
Summary of the water transport (Sv) through the main straits in the SCS based on observation and numerical data (positive is inflow).

	Luzon Strait	Taiwan Strait	Karimata Strait	Mindoro Strait
Observation	4.8 (winter; Yaremchuk and Qu, 2004); (UPPER LAYER)	0.1 (winter, Jan et al., 2006);	−2.7 ± 1.1 (winter., Susanto et al., 2013);	−2.4 (Qu et al., 2009)
	4.2-5 (annual, Su, 2004); (UPPER LAYER)	0.12 ± 0.33 (winter, Lin et al., 2005);		
	3 (annual, Liang et al., 2003); (UPPER LAYER)			
	5 (Jul) and −9 (Oct.) (Tian et al., 2006).(UPPER LAYER)			
	3.5 (Jul., Yang et al., 2010); (UPPER LAYER, GEOSTROPHIC FLOW)			
	−2.5 (Jul) and 5 (Oct.) (Tian et al., 2006).(MIDDLE LAYER)			
	−5 (Jul., Yang et al., 2010); (MIDDLE LAYER, GEOSTROPHIC FLOW)			
	2 (Jul) and −2 (Oct.) (Tian et al., 2006).(DEEP LAYER)			
	1 (Jul., Yang et al., 2010); (DEEP LAYER, GEOSTROPHIC FLOW)			
Numerical estimation	3.1 (winter, Rong et al., 2007); (UPPER LAYER)	0–0.4 (winter, Jan et al., 2002)	−2.26(annual, Cai et al., 2005);	–
	8.1 (winter, Zhao et al., 2009); (UPPER LAYER)	1.09 (annual, Wu and Hsin, 2005)	−1.16 (annual, (Fang et al., 2009)	−3.2 (annual, Gan et al., 2016)
	7.6 (winter, Wang et al., 2009); (UPPER LAYER)		−1.42 (annual, Liu et al., 2011)	
	4 (winter, Yaremchuk et al., 2009); (UPPER LAYER)			
	5.9 (annual, Gan et al., 2016); (UPPER LAYER)			
	−1.4 (annual, Gan et al., 2016); (MIDDLE LAYER)			
	0.9 (annual, Gan et al., 2016); (DEEP LAYER)			

where T_a is the near-surface atmospheric temperature; T_o is the SST; α and β are the exchange coefficients associated with the heat capacity of the atmosphere and ocean, respectively ($\alpha \gg \beta$); γ_a and γ_o are the radiative damping coefficients; and N_a and N_o represent stochastic forcing. If the forcing arises only in the atmosphere, $N_a \neq 0$, and $N_o = 0$. Wu et al. (2006) demonstrated that when atmosphere forcing dominates, the SST tendency and SHF have a significant negative relationship, and the correlation between T_o and SHF is small. Conversely, when ocean forcing dominates, the correlation between SST tendency ($\frac{dT_o}{dt}$) and SHF is small and that between T_o and SHF, $\alpha(T_o - T_a)$, is positive (von Storch, 2000; Wu et al., 2006). Related studies have shown that thermal inertial waves in the upper ocean generally serve to integrate high-frequency atmospheric weather, forcing an SST response (von Storch, 2000; Park et al., 2005; Wu et al., 2006). However, Bishop et al. (2017) noted that enhanced ocean advection features, such as fronts and mesoscale eddies, can result in the dominance of ocean forcing.

Fig. 9 illustrates the modeled relationship between SST (or SST tendency) anomalies and SHF anomalies during the El Niño and La Niña winter (December–February) and spring (March–May), respectively. The anomalies are calculated by subtracting the climatological monthly mean (NCEP reanalysis 1979–2009). During the El Niño winter, atmospheric forcing dominates the anomalous SHF variation in the northern and central parts of the SCS (Fig. 9a and b). Anomalous low-level anticyclonic circulation over the SCS (Fig. 5) suppresses convection and upward heat flux, resulting in atmospheric forcing dominance. During the La Niña winter, although atmospheric forcing predominates in the SCS, the ocean forces anomalous air–sea heat flux in some regions, including off the China coast and southwest of Taiwan in the northern SCS and in the cyclonic mesoscale eddy region in the southern SCS (Fig. 9c and d). The cold China coastal current intensifies the cool water advection in the northern SCS. In addition, an anomalous cyclonic upper ocean circulation in the southern SCS provides a relatively strong advective ocean heat flux from the south, resulting in SST-forced atmospheric feedback in the southern SCS.

During the El Niño spring (March–May), the atmosphere forces the SST except to the east of Vietnam (Fig. 9e and f). Similar results are obtained for the La Niña spring except in the region of the SST forcing the shifts southward (Fig. 9g and h); this location shift also occurs in the difference in the upper ocean currents (Fig. 6i and j). In this region, the advective heat flux caused by the ocean current is important (Xie et al., 2007; Li et al., 2014), and the SST forces the anomalous air–sea heat flux variation.

3.4. SCS subsurface response to the ENSO

3.4.1. Modulation of MLDs and related mesoscale features in the SCS

The subsurface response of the SCS to ENSO variability plays a crucial role in the air–sea interaction and the water and heat exchange between the SCS and other ocean basins. Fig. 10a and b depict the winter (December–February) and spring (March–May) mean MLDs during 2015–2016, respectively. The MLD is defined as the depth at which the temperature is 0.5 °C lower than at the surface (Levitus, 1982). During winter, the western boundary current in the SCS has a relatively large MLD (Fig. 10a). Because the strengthening of the western boundary current enhances the vertical shear, the enhanced downward momentum flux and vertical mixing increase the MLDs. In the region 110°–112°E, 12°–16°N, the larger MLDs are associated with an anticyclonic circulation located to the north of the cyclonic circulation in the upper layer of the southern SCS (Fig. 3h–j). These circulation patterns are commonly found in the SCS in winter (Hu et al., 2000). During spring, the MLDs are smaller because of relaxation of the winter monsoon (Fig. 10b), which contributes to the change in vertical mixing and large surface heating. Slightly greater MLDs are observed in the Kuroshio loop in the Luzon Strait and anticyclonic eddy to the east of Vietnam, as expected.

Fig. 10(c) and (d) further show the corresponding difference in MLD between El Niño and La Niña; the differences in surface wind stress curl between El Niño and La Niña are superimposed as contours. The MLDs in the El Niño winter are generally greater than in the La Niña winter, particularly in the southern SCS, off the shore of southwestern Taiwan, and in the western boundary current. The MLD difference in the southern SCS is directly related to the negative surface wind stress curl and strength of the cyclonic mesoscale eddy in the area. A strong cyclonic eddy is accompanied by a small MLD. During the winter of the El Niño (La Niña) year, the southward water transport along the western boundary of the SCS is reduced (enhanced) (Fig. 6g–h),

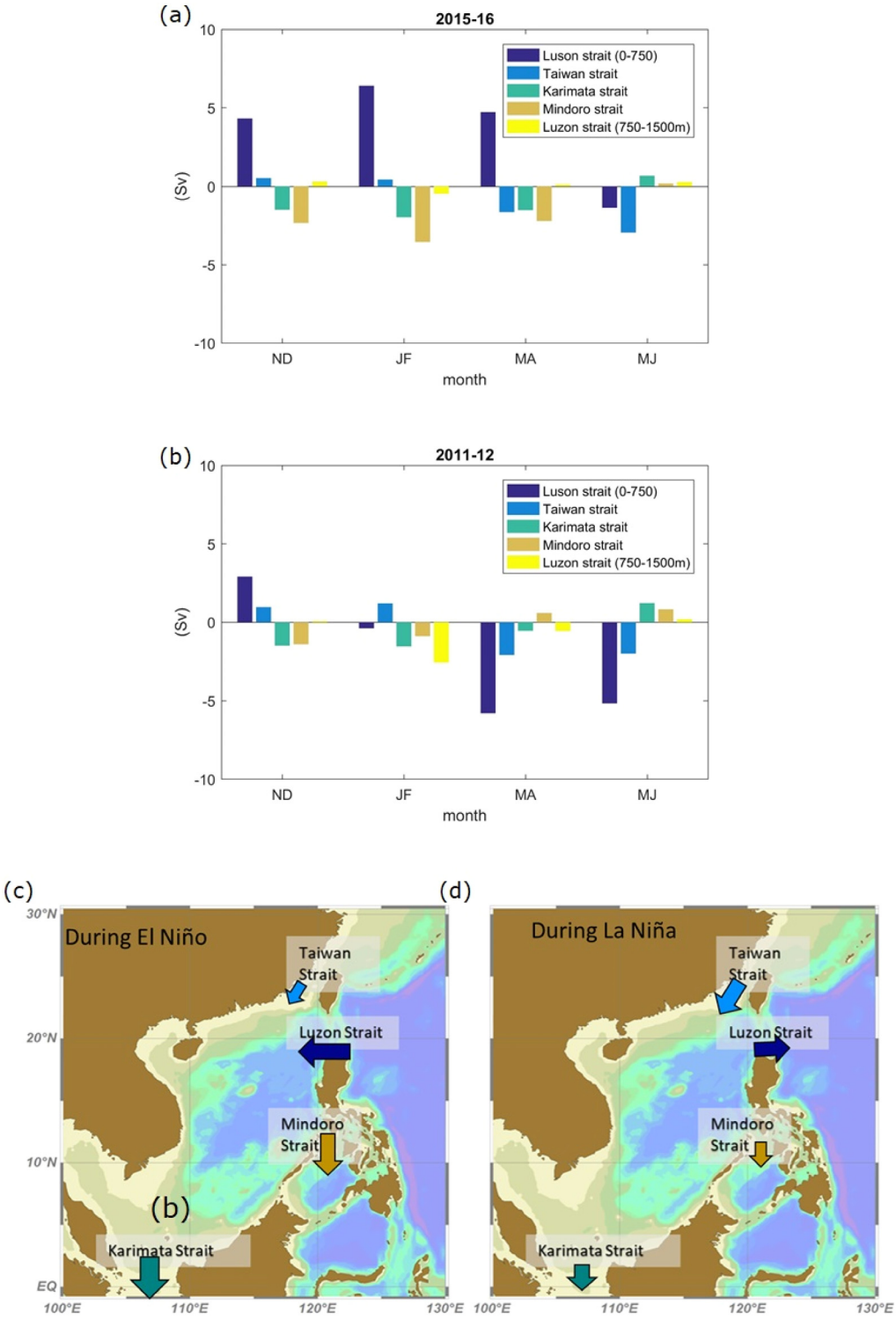

Fig. 13. The 2-month averaged water budget of SCS (inflow is positive) during (a) El Niño and (b) La Niña. (c)–(d) Schematic of the comparison in anomalies of water transport through the main straits between El Niño and La Niña.

which decreases (increases) the planetary vorticity flux in the southern SCS; consequently, the cyclonic eddy in the southern SCS is weakened (intensified). Off the shore of China, the relatively large MLDs in the El Niño winter are accompanied by a weaker coastal current than in the La Niña winter, which cannot be explained by the difference in positive wind stress curl (Fig. 10c). The mechanism responsible for the greater MLDs in this region is associated with wind–current–topography interaction. Fig. 11 shows the composite of MLDs from eight ENSO events using the HYCOM reanalysis (GOFS 3.1). The results show similar pattern to those in Fig. 10, except a weaker magnitude, confirming the robustness of these features.

Fig. 12 shows the time-averaged (December–February) temperature (shaded) and v-velocity (contours) along 114°E, 18°–23°N. The stronger (weaker) horizontal convergence off the southern coast of China, due to the stronger (weaker) Ekman flow during the La Niña (El Niño) winter, drives more (less) cool bottom water offshore, cooling

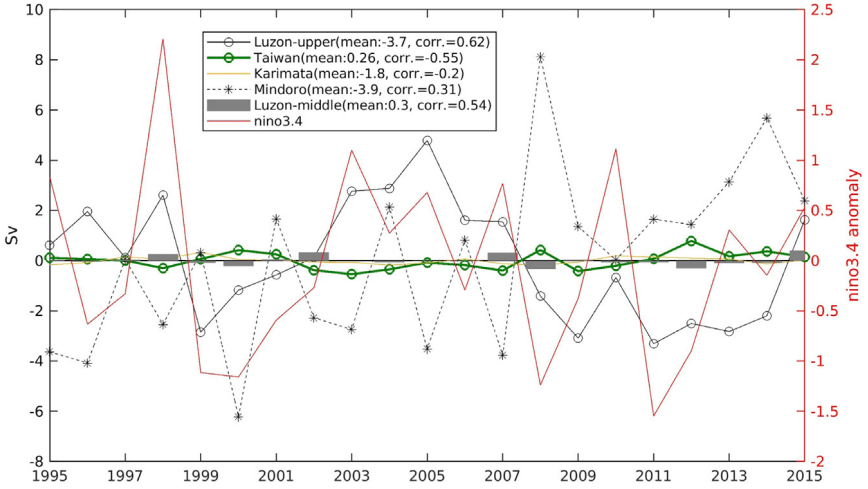

Fig. 14. Interannual variation of the water transport anomalies (positive: inflow) during winter (Nov–Feb) for the four straits calculated using HYCOM reanalysis (GOFS 3.1: 41-layer HYCOM + NCODA Global 1/12° Reanalysis, 1994–2015). The mean transport and the correlation with Niño3.4 are included in the legend.

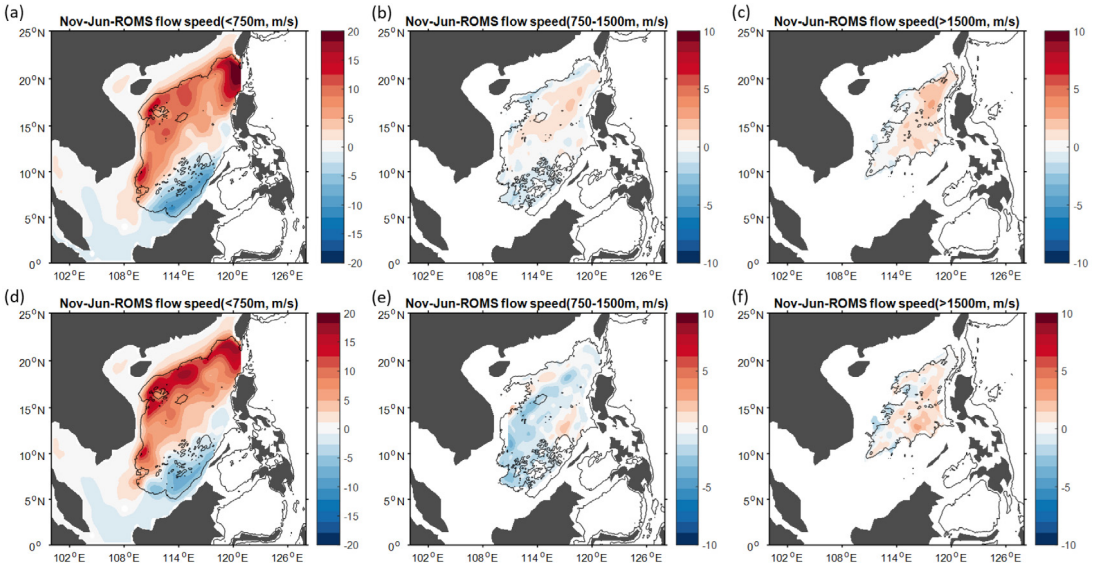

Fig. 15. 8-month averaged stream functions (Sv) in the upper (<750 m), middle (750–1500 m), and bottom layers (>1500 m) in SCS during (a)–(c) El Niño and (d)–(f) La Niña.

the subsurface in the offshore region (process schematic presented in Fig. 12). The pattern of MLD difference during spring is similar to that for winter but with considerably lower magnitude.

3.4.2. Modulation of water exchange in the SCS

Climatologically, the major water exchange that occurs in the SCS is that through the inflow Luzon Strait to the north, and the outflow is through the Mindoro and Karimata Straits to the south (Qu et al., 2009). The Luzon Strait is the only deep strait that connects the middle and deep layers of the SCS to the other basins. Annually, the following three-layer structure of Luzon Strait transport is observed: upper-layer inflow, middle-layer inflow, and deep-layer inflow (Hsin et al., 2012; Xu and Oey, 2014). However, during the spring and summer, the Luzon Strait inflow commonly decreases because the Kuroshio mainstream shifts eastward across the Luzon Strait (Liang et al., 2008), causing the northern SCS current to flow eastward across the northern Luzon Strait (outflow) in summer (Hsin et al., 2012). Although the annual mean water transport in the Taiwan Strait is northward (outflow), in winter, the transport turns southward because of driving by the strong northeasterly monsoon (Jan et al., 2006). Table 1 summarizes the water transport through the main straits in the SCS on the basis of observation and numerical data.

Figs. 13a and 14b compare the 2-month-averaged water transport through the four main straits (labeled in Fig. 1) connecting the SCS with other basins during the two ENSO years. A schematic of water transport through the main straits between the El Niño and La Niña is also provided (Fig. 13c and d). The inflow through Taiwan Strait during El Niño winter is considerably weaker than in La Niña winter, resulting from a reduced northeasterly monsoon associated with the anticyclonic atmospheric circulation (Fig. 5).

The Luzon Strait inflow is considerably larger during El Niño than La Niña and is accompanied by a higher and lower increase of outflow through the Mindoro Strait and Karimata Strait, respectively. The Mindoro Strait outflow has been reported to be strongly correlated with the Luzon Strait inflow (Metzger and Hurlburt, 1996). As expected, the outflow through the middle layer of the Luzon Strait is weaker during El Niño (Fig. 13). To further explore the long-term impact of the ENSO on water transport through the SCS, we quantify the winter water transport (November–February) in the four straits between 1994 and 2015 using the HYbrid Coordinate Ocean Model (HYCOM) reanalysis data [GOFS 3.1: 41-layer HYCOM + Navy Coupled Ocean Data Assimilation (NCODA) Global 1/12° Reanalysis; Fig. 14]. The interannual transport in the upper and middle layers of the Luzon

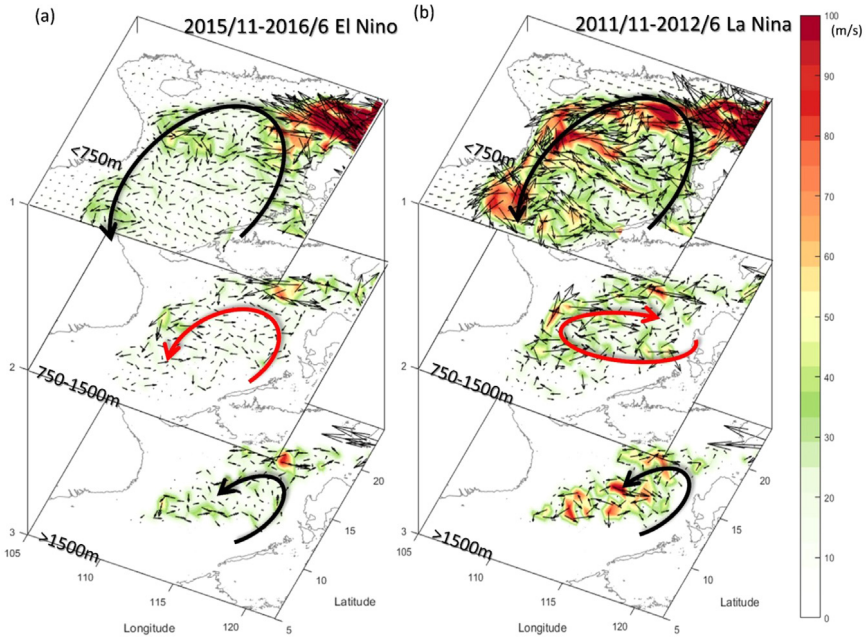

Fig. 16. 8-month averaged (Nov–Jun) circulation pattern in the SCS during (a) El Niño and (b) La Niña. Color shading indicates the flow rate (m^3/s).

Strait varies considerably with ENSO variability (correlations of 0.62 and 0.54, respectively). The correlation between the Taiwan Strait and nino3.4 is −0.55, suggesting similar ENSO effects due to the low-level surface wind changes. However, the transport in the Mindoro Strait is not strongly correlated with the ENSO. Overall, the interannual water transport is consistent with the schematic presented in Fig. 13(c) and (d). The HYCOM reanalysis uses data assimilation with in situ and satellite observations.

This relatively large inflow through the Luzon Strait during El Niño is associated with enhanced Kuroshio intrusion. Previous studies have suggested that the Kuroshio Current loops into the Luzon Strait, and its strength is mainly determined by the upstream Kuroshio speed, local wind stress, and mesoscale eddies (Yuan et al., 2006; Sheremet and Kuehl, 2007; Hsin et al., 2012). Considering only the ENSO-related wind variability, the reduced northeasterlies during El Niño favor an eastward shift of the Kuroshio mainstream in the Luzon Strait. Hence, the local wind stress is not responsible for the enhanced Kuroshio intrusion. The lower or higher upstream Kuroshio speed is responsible for the enhanced or weakened Kuroshio loop, respectively, in the Luzon Strait. The volume transport at 0–700 m off the eastern coast of Luzon Island (18°N, 121°–124°E) averaged over 8 months (November–June) during La Niña is 5.51Sv larger than that during El Niño. For a western boundary current encountering a boundary gap, such as the Kuroshio Current in the Luzon Strait, the vorticity balance is dominated by the advection and β terms. When the upstream Kuroshio speed is small enough such that the β effect dominates the flow, the Kuroshio Current tends to intrude westward into the northern SCS and then drastically returns, forming an intense loop that preserves the potential vorticity with a strong curved flow (Sheremet and Kuehl, 2007; Kuehl and Sheremet, 2009). The interannually varying water transport off the eastern coast of Luzon Island is correlated with the northward or southward shift of the North Equatorial Current (NEC) bifurcation, which is the origin of the Kuroshio Current (Fig. 1). The southward migration of the NEC bifurcation latitude results in an intensified Kuroshio Current east of Luzon Island (Yuan et al., 2014). Kim et al. (2004) suggested that this relationship is mainly due to westward propagation of upwelling (downwelling) Rossby waves generated by winds in the central equatorial Pacific and by an anomalous low-level anticyclone (cyclone) located in the western North Pacific during El Niño (La Niña). Qiu and Chen (2010) discovered that the latitude of NEC bifurcation is determined by the surface wind forcing (wind stress and its curl) in the 12°–14°N band in the western Pacific basin, and the associated anomalies are significantly influenced by the ENSO. The westerlies (easterlies) and positive (negative) wind stress curl anomalies during El Niño (La Niña) cause divergence (convergence) in the upper ocean that lowers (increases) the sea level height and are accompanied by northward (southward) movement of the latitude of NEC bifurcation.

3.4.3. Three-dimensional circulation in the SCS

The ocean circulation in the SCS generally consists of a three-layer structure (top to bottom: cyclonic, anticyclonic, and cyclonic). Using the reduced-gravity equations, Xu and Oey (2014) deduced that the cyclonic circulation in the upper layer results from wind-induced Ekman pumping and potential vorticity fluxes through the Luzon and Mindoro Straits. The Mindoro Strait offsets the influx from the Luzon Strait. Because the influence of the anomalous wind stress is mostly confined to the upper ocean and the Luzon Strait is the only channel deep enough to connect the middle layer of the SCS with the Pacific Ocean, the middle-layer transport of the Luzon Strait controls the circulation anomalies in the middle layer of the SCS. The basin's middle-layer (570–2000 m) circulation is anticyclonic because of the outflow transport through the Luzon Strait. Gan et al. (2016) deduced the dominant term for the circulation is the vortex stretching. The major source of vortex stretching is the negative planetary vorticity flux extrinsically induced by the outflow in the middle layer (750–1500 m) through the Luzon Strait.

Fig. 15 depicts the layer-integrated transport stream function in the upper (<750 m), middle (750–1500 m), and lower (>1500 m) layers during El Niño and La Niña. This followed the definition of Gan et al. (2016). Fig. 16 presents a comparison of the three-layer flow rate (m^3/s) patterns between El Niño and La Niña. In the upper layer, both circulation patterns are cyclonic, similar to the climatological mean. However, the circulation is weaker during the El Niño year than the La Niña year. In the middle layer, an anomalous cyclonic circulation is discovered during El Niño Fig. 15a). The anomalous cyclonic circulation in the middle layer is consistent with the water exchange through the main straits around the SCS (Xu and Oey, 2014; Gan et al., 2016). The planetary vorticity influx accompanied by the enhanced Kuroshio intrusion into the SCS is the major source of anomalous cyclonic

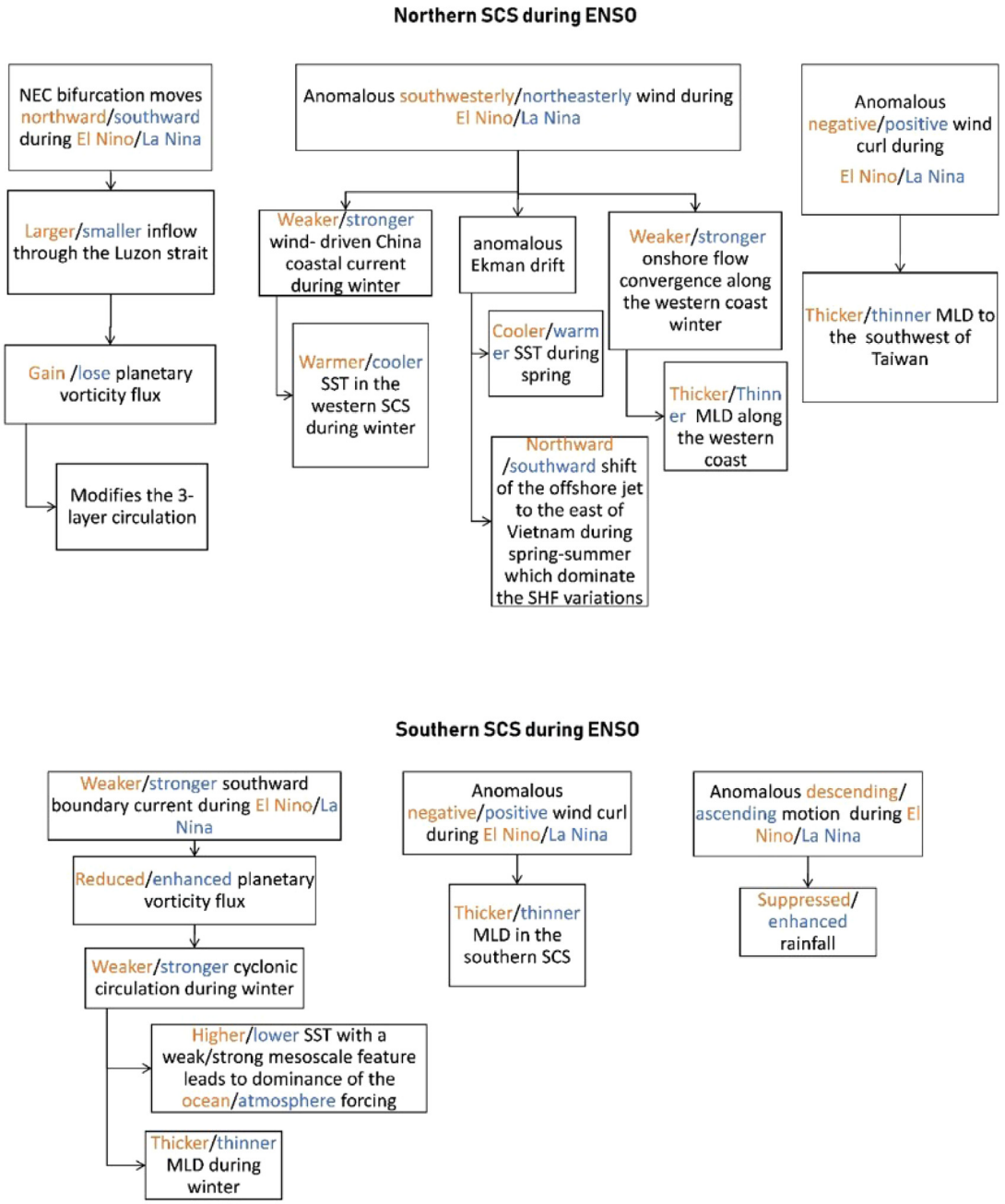

Fig. 17. Summary of the ENSO impacts on the northern and southern SCS and the corresponding processes.

circulation in the upper and middle layers during El Niño (November–June). The anomalous cyclonic circulation in the SCS's middle layer is attributed to the increased middle-layer inflow in the Luzon Strait. In the lower layer, cyclonic circulation exists in both events, consistent with the climatological mean structure. The ENSO's influence on deep layer circulation is weak compared with that on the upper and middle layers.

4. Discussion and conclusion

We used a high-resolution regional coupled model to understand the crucial roles of oceanic mesoscale features in the air–sea interaction and subsurface ocean response during the ENSO and its decay. The relative importance of atmospheric and oceanic forcing in the SST change in different regions of the SCS was also addressed. We revealed that an anomalous anticyclonic (cyclonic) circulation in the low-level atmosphere strongly affects the surface and subsurface patterns of the SCS during El Niño (La Niña). Particularly, the response of the SCS differs between regions. Fig. 17 details the dynamical processes underlying the impact of the ENSO on the northern and southern SCS.

In the northern SCS, the anomalous anticyclonic circulation in the low-level atmosphere suppresses the upward STHF during an El Niño winter; however, the anomalous Ekman drift (toward the southwest) near the coast causes anomalous ocean surface cooling. The combination of weakened upward STHF (warming) and a weaker southward western boundary current (cooling) results in a net higher SST in the northwestern SCS. This phenomenon is reversed during a La Niña winter. During an El Niño and La Niña spring, displacement of the Vietnam coastal jet can trigger an SST-forced atmosphere condition. Both wind stress curl anomalies and the wind–flow–topography interaction play critical roles in the change in MLD (Figs. 10–12). In addition, enhanced Kuroshio intrusion during El Niño, which is associated with northward

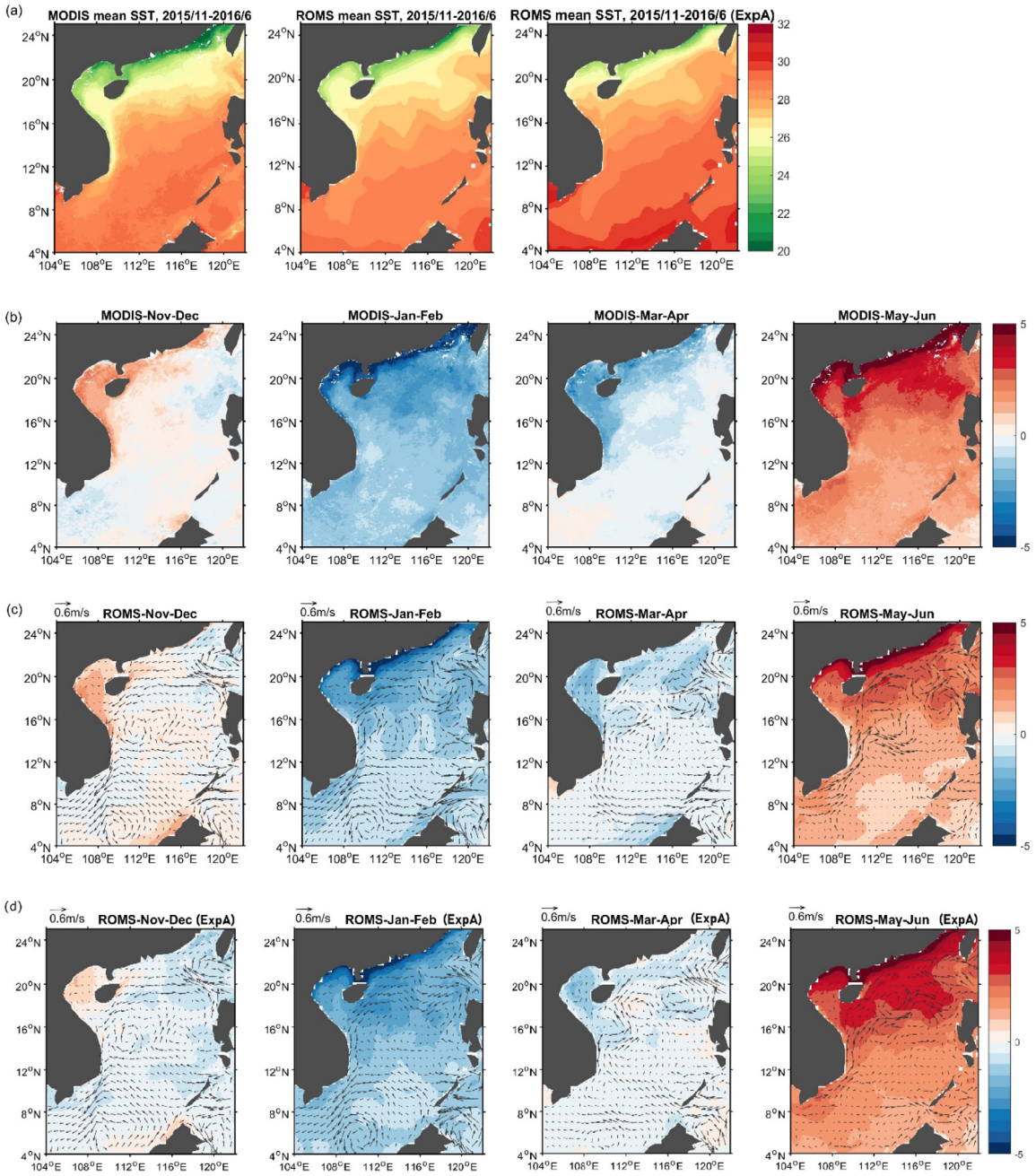

Fig. A.1. (a) The 8-month averaged (2015/11-2016/6) SST from MODIS, original model run and ExpA1, and the 2-month averaged (Nov–Dec, Jan–Feb, Mar–Apr, May–Jun) of the MODIS SST deviated from the 8-month average from (b) MODIS SST (b) original model run and (c) ExpA1. The averaged surface currents are superimposed as vectors.

movement of the NEC bifurcation, results in water exchange between the SCS and the western Pacific, modifying the circulation pattern in the SCS.

In the southern SCS, the anomalous low-level anticyclonic atmospheric circulation suppresses convection and rainfall in the southern SCS during El Niño winter to spring. Simultaneously, the commonly observed cyclonic upper ocean circulation is weakened and the MLD is decreased during El Niño; this is associated with a weaker wind-driven western boundary current and anomalous negative wind stress curl. The weakened western boundary current and cyclonic circulation associated with the ENSO alter the relative oceanic and atmospheric contributions to energy exchange across the air–sea interface, leading to a complex scenario that cannot be easily explained using the typical low-resolution coupled global circulation model (Section 3.3.2). Finally, the SST forces SHF anomalies off the shore of China during La Niña winter. Our results clarify many regional air–sea coupling issues in the SCS.

Declaration of competing interest

The authors declare that they have no known competing financial interests or personal relationships that could have appeared to influence the work reported in this paper.

Acknowledgments

The constructive comments from the anonymous reviewers are greatly appreciated. This study is supported by the Ministry of Science

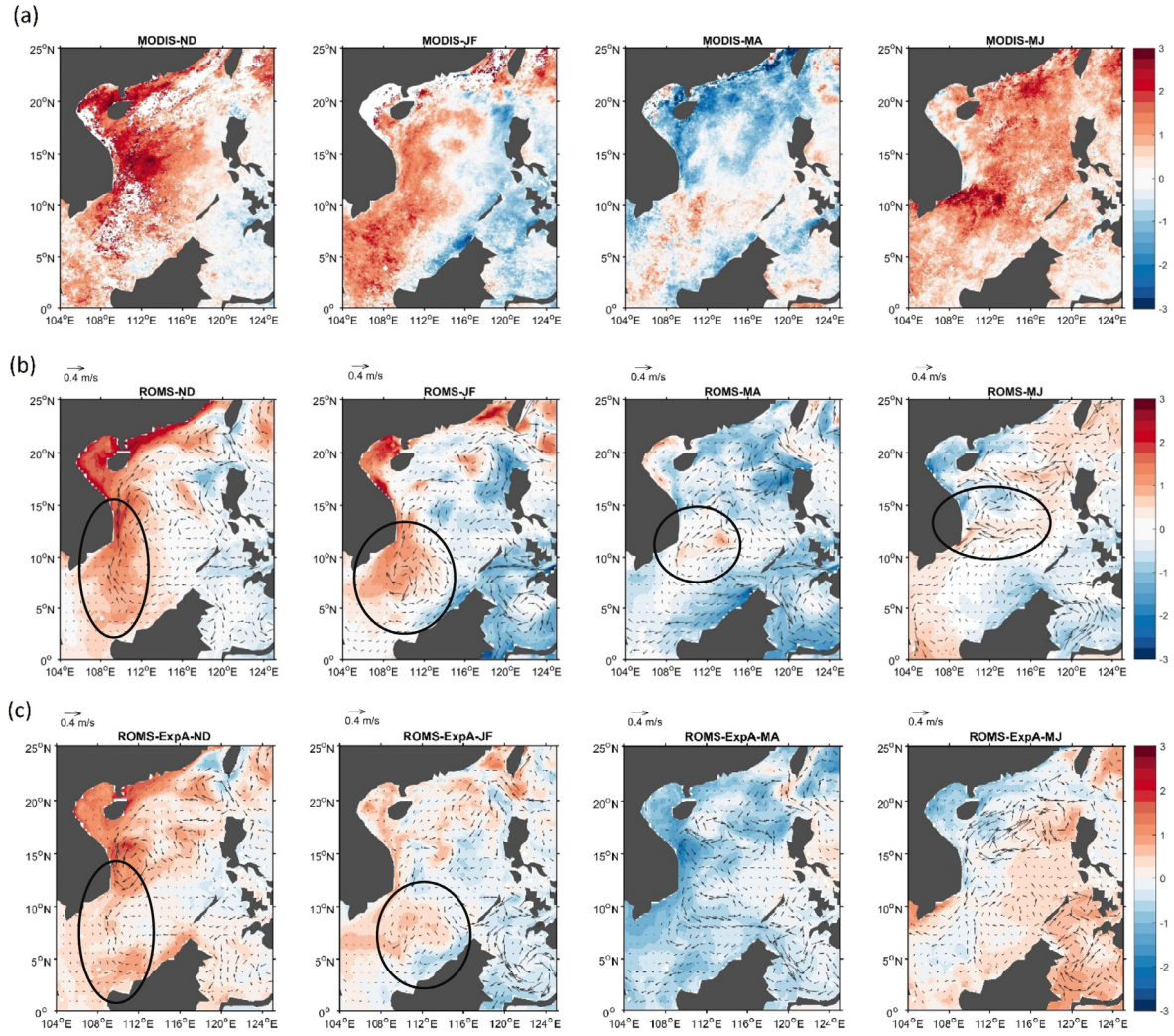

Fig. A.2. 2-month mean differences in SST and surface current between the El Niño and La Niña cases using results from (a) the MODIS satellite measurements, (b) the original couple runs, and (c) ExpA1 and A2. The important mesoscale feature such as the northward flow difference in the western boundary current region, the anomalous anticyclonic circulation and the northward shift of the offshore jet off Vietnam are marked by the black circles.

and Technology (MOST), Taiwan. Grant # 107 – 2611 – M – 002 – 013 – M Y4 and 108 – 2111 – M – 002 – 006 –MY3.

Appendix

In the ExpA1 and ExpA2 (Table A.1), the ROMS model is forced by the ERA-Interim reanalysis without coupling with the WRF model. The 3-hourly surface data with a resolution of 80 km is retrieved from https://apps.ecmwf.int/datasets/data/interim-full-daily/levtype=sfc/. The monthly averaged surface winds from the ERA-Interim is similar to the NCEP reanalysis (figure not shown). By comparing these runs with the original coupled simulations, we can clearly examine the ocean response differences driven by a more correct surface forcing. However, we note that the air–sea coupling process (e.g. Fig. 9) is missing in the additional runs.

Fig. A.1 compares the sea surface temperature and current from the satellite observation, the coupled run, and the forced run (Exp A1) during El Niño. The 8-month mean patterns are generally similar among them. The Kuroshio intrusion into the SCS accompanying with high SST west of the Luzon Strait is evident. The forced ExpA1 has warmer SST than the coupled run, especially in the southern SCS. But, the western boundary current and enhanced Kuroshio intrusion is similar to the coupled run. The 2-month averaged deviation also shows similar patterns but slightly different magnitudes. Particularly, during May–June, ExpA1 shows higher SST in the northern SCS (Fig. A.1d) than the coupled run (Fig. A.1c). In the 8-month mean pattern (Fig. A.1a), ExpA1 also shows higher SST than the MODIS observation. These results suggest that the SST is overestimated during May–June in the forced run. The surface currents are similar in both the coupled and Exp A1 runs; including the southward western boundary current, the cyclonic circulation in the southern SCS and the Kuroshio intrusion into the northern SCS. After spring, the western boundary current reverses in both runs while the offshore current to the east of Vietnam in the ExpA1 is weaker with southward shift.

Fig. A.2(a–c) compares 2-month mean differences in SST and surface current between El Niño and La Niña in the MODIS, coupled run, and ExpA, respectively. The winter SST difference in the ExpA is weaker than that in the coupled run and the MODIS observation. Also, the spatial pattern of the March–April SST difference (northern and southern SCS) in the coupled run is closer to the MODIS than the difference of Exp A. The second-time warming during May–June is slightly stronger in the Exp A (but still weaker than the MODIS). Similarly, the surface current differences show consistent mesoscale features in the coupled and forced ExpA runs before Spring (the consistent northward flow difference in the western boundary region and the anticyclonic difference in the southern SCS marked by the circles in Fig. A.2). However, after Spring, the surface current difference to the east of Vietnam, associated

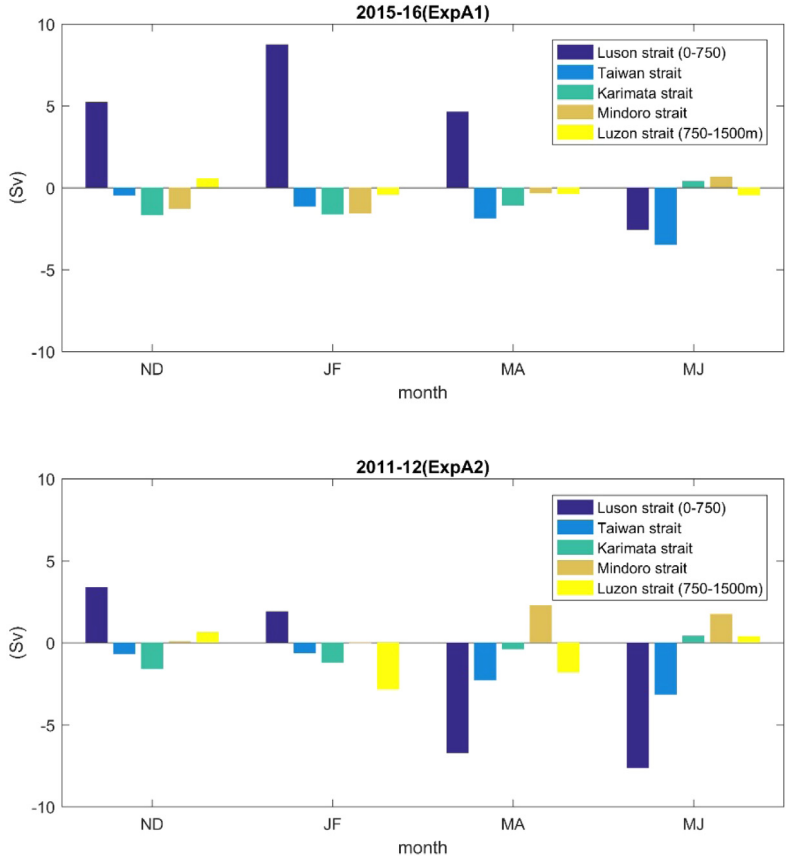

Fig. A.3. The 2-month averaged water budget of SCS (inflow is positive) during (a) El Niño and (b) La Niña in ExpA1 and A2, respectively.

Table A.1
The original and additional model runs setting.

	Ocean	Atmosphere	Couple
Original run — El Niño	ROMS 2015/11 – 2016/2	WRF model	Atm.↔Ocn
Original run — La Niña	ROMS 2011/11 – 2012/2	WRF model	Atm.↔Ocn
ExpA1 — El Niño	ROMS 2015/11 – 2016/2	ERA-Interim	Atm.→Ocn
ExpA2 — La Niña	ROMS 2011/11 – 2012/2	ERA-Interim	Atm.→Ocn

with the northward/southward shifting of the offshore jets during El Niño/La Niña is absent in the forced ExpA. This shift of the offshore jets can be found from the HYCOM reanalysis composite (Fig. 6n) and has been noted in Li et al. (2014). These results suggest that either the spatial resolution of the wind-forcing (~80 km in the ExpA versus ~12 km in the coupled run) or the air–sea coupling process might play an important role in the displacement of the eastward jet, which is an interesting topic but beyond the scope of this study.

Fig. A.3 further shows the 2-month averaged water budget of SCS (inflow is positive) in ExpA1 and ExpA2. The similar budgets to the original coupled runs (Fig. 13) suggest that the dynamics and differences between these two ENSO events are consistent, as shown in Fig. 13c–d. Overall, the general ocean responses in SCS in the additional experiments suggest that the slightly displaced anticyclonic circulation (westward shift) in the coupled model does not affect the robust ocean responses.

References

Bishop, S.P., Small, R.J., Bryan, F.O., Tomas, R.A., 2017. Scale dependence of midlatitude air–sea interaction. J. Clim. 30, 8207–8221.
Cai, S.Q., Liu, H.L., Li, W., Long, X.M., 2005. Application of LICOM to the numerical study of the water exchange between the South China Sea and its adjacent oceans. Acta Oceanol. Sin. 24, 10–19.
Chao, S.Y., Shaw, P.T., Wu, S.Y., 1996. El Niño modulation of the South China sea circulation. Prog. Oceanogr. 38, 51–93.
Chen, J., Wang, X., Zhou, W., Wen, Z., 2018. Interdecadal change in the summer SST-precipitation relationship around the late 1990s over the South China Sea. Clim. Dynam. 51, 2229–2246.
Chu, P.C., Chang, C.P., 1997. South China Sea warm pool in boreal spring. Adv. Atmos. Sci. 14, 195–206.
Dai, A., 2016. Historical and future changes in streamflow and continental runoff: A review. In: Tang, Qiuhong, Oki, Taikan (Eds.), Terrestrial Water Cycle and Climate Change: Natural and Human-Induced Impacts. In: Geophysical Monograph, vol. 221, AGU, John Wiley Sons, pp. 17–37 (Chapter 2).
Fang, G., Fang, W.D., Fang, Y., Wang, K., 1998. A survey of studies on the South China Sea upper ocean circulation. Acta Oceanogr. Taiwan. 37, 1–16.
Fang, G., Wang, Y., Wei, Z., Fang, Y., Qiao, F., Hu, X., 2009. Interocean circulation and heat and freshwater budgets of the South China Sea based on a numerical model. Dyn. Atmos. Oceans 47, 55–72.
Gan, J., Liu, Z., Hui, C.R., 2016. A three-layer alternating spinning circulation in the South China Sea. J. Phys. Oceanogr. 46, 2309–2315.
He, Z., Wu, R., 2013. Seasonality of interannual atmosphere–ocean interaction in the South China Sea. J. Oceanogr. 69, 699–712.
Hoerling, M.P., Kumar, A., Zhong, M., 1997. El Niño, La Niña, and the nonlinearity of their teleconnections. J. Clim. 10, 1769–1786.
Hsin, Y.C., Wu, C.R., Chao, S.Y., 2012. An updated examination of the Luzon Strait transport. J. Geophys. Res.: Oceans 117, C03022.
Hu, J., Kawamura, H., Hong, H., Qi, Y., 2000. A review on the currents in the South China Sea: seasonal circulation, South China Sea warm current and Kuroshio intrusion. J. Oceanogr. 56, 607–624.
Hu, Z.Z., Kumar, A., Zhu, J., Huang, B., Tseng, Y.H., Wang, X., 2017. On the shortening of the lead time of ocean warm water volume to ENSO SST since 2000. Sci. Rep. 7, 4294.
Jan, S., Sheu, D.D., Kuo, H.M., 2006. Water mass and throughflow transport variability in the Taiwan Strait. J. Geophys. Res.: Oceans 111, C12012.
Jan, S., Wang, J., Chern, C.S., Chao, S.Y., 2002. Seasonal variation of the circulation in the Taiwan Strait. J. Mar. Syst. 35, 249–268.
Kim, Y.Y., Qu, T., Jensen, T., Miyama, T., Mitsudera, H., Kang, H.W., Ishida, A., 2004. Seasonal and interannual variations of the North Equatorial Current bifurcation in a high-resolution OGCM. J. Geophys. Res.: Oceans 109 (C3).
Kuehl, J.J., Sheremet, V.A., 2009. Identification of a cusp catastrophe in a gap-leaping western boundary current. J. Mar. Res. 67, 25–42.

Lau, N.C., Nath, M.J., 2009. A model investigation of the role of air–sea interaction in the climatological evolution and ENSO-related variability of the summer monsoon over the South China Sea and western North Pacific. J. Clim. 22, 4771–4792.
Levitus, S., 1982. Climatological Atlas of the World Ocean, NOAA Prof. Pap., Vol. 13. U.S. Govt. Printing Off., Washington, D. C., p. 173.
Li, Y., Han, W., Wilkin, J.L., Zhang, W.G., Arango, H., Zavala-Garay, J., Levin, J., Castruccio, F.S., 2014. Interannual variability of the surface summertime eastward jet in the South China Sea. J. Geophys. Res.: Oceans 119, 7205–7228.
Li, T., Wang, B., Wu, B., et al., 2017. Theories on formation of an anomalous anticyclone in western North Pacific during El Niño: A review. J. Meteorol. Res. 31 (6), 987–1006. http://dx.doi.org/10.1007/s13351-017-7147-6.
Liang, W.-D., Tang, T.Y., Yang, Y.J., Ko, M.T., Chuang, W.-S., 2003. Upper-ocean currents around Taiwan. Deep-Sea Res. II 50, 1085–1105.
Liang, W.D., Yang, Y.J., Tang, T.Y., Chuang, W.S., 2008. Kuroshio in the Luzon Strait. J. Geophys. Res.: Oceans 113, C08048.
Lin, S.-F., Tang, T.-Y., Jan, S., Chen, C.-J., 2005. Taiwan Strait current in winter. Cont. Shelf Res. 25, 1023–1042.
Liu, Q., Feng, M., Wang, D., 2011. ENSO-induced interannual variability in the southeastern South China Sea. J. Oceanogr. 67, 127–133.
Liu, Q.-Y., Wang, D., Wang, X., Shu, Y., Xie, Q., Chen, J., 2014. Thermal variations in the South China Sea associated with the eastern and central Pacific El Niño events and their mechanisms. J. Geophys. Res.: Oceans 119, 8955–8972.
Metzger, E.J., Hurlburt, H.E., 1996. Coupled dynamics of the South China sea, the Sulu sea, and the Pacific ocean. J. Geophys. Res.: Oceans 101 (C5), 12331–12352.
Miller, A.J., Collins, M., Gualdi, S., Jensen, T.G., Misra, V., Pezzi, L.P., Pierce, D.W., Putrasahan, D., Seo, H., Tseng, Y.H., 2017. Coupled ocean–atmosphere modeling and predictions. J. Mar. Res. 75, 361–402.
Park, S., Deser, C., Alexander, M., 2005. Estimation of the surface heat flux response to sea surface temperature anomalies over the global oceans. J. Clim. 18, 4582–4599.
Qiu, B., Chen, S., 2010. Interannual-to-decadal variability in the bifurcation of the North Equatorial Current off the Philippines. J. Phys. Oceanogr. 40, 2525–2538.
Qu, T., 2000. Upper-layer circulation in the South China Sea. J. Phys. Oceanogr. 30 (6), 1450–1460.
Qu, T., Kim, Y.Y., Yaremchuk, M., Tozuka, T., Ishida, A., Yamagata, T., 2004. Can Luzon Strait transport play a role in conveying the impact of ENSO to the South China Sea? J. Clim. 17, 3644–3657.
Qu, T., Song, Y.T., Yamagata, T., 2009. An introduction to the South China Sea throughflow: Its dynamics, variability, and application for climate. Dyn. Atmos. Oceans 47, 3–14.
Rong, Z., Liu, Y., Zong, H., Cheng, Y., 2007. Interannual sea level variability in the South China Sea and its response to ENSO. Glob. Planet. Change 55, 257–272.
Sheremet, V.A., Kuehl, J., 2007. Gap-leaping western boundary current in a circular tank model. J. Phys. Oceanogr. 37, 1488–1495.
Skamarock, W.C., Klemp, J.B., Dudhia, J., Gill, D.O., Barker, D.M., Wang, W., Powers, J.G., 2005. A Description of the Advanced Research WRF Version 2. NCAR Technical Note NCAR/TND468+STR, Available at http://www.mmm.ucar.edu/wrf/users/docs/arwv2.pdf.
Su, J., 2004. Overview of the South China Sea circulation and its influence on the coastal physical oceanography outside the Pearl River Estuary. Cont. Shelf Res. 24, 1745–1760.
Susanto, R.D., Wei, Z., Adi, R.T., Fan, B., Li, S., Fang, G., 2013. Observations of the Karimata Strait througflow from 2007 to 2008. Acta Oceanol. Sin. 32, 1–6.
Tan, W., Wang, X., Wang, W., Wang, C., Zuo, J., 2016. Different responses of sea surface temperature in the South China sea to various El Niño events during boreal autumn. J. Clim. 29 (3), 1127–1142.
Tian, J., Yang, Q., Liang, X., Xie, L., Hu, D., Wang, F., Qu, T., 2006. Observation of Luzon Strait transport. Geophys. Res. Lett. 33 (19).
von Storch, J.-S., 2000. Signatures of air–sea interaction in a coupled atmosphere–ocean GCM. J. Clim. 13, 3361–3379.
Wang, Q., Cui, H., Zhang, S., Hu, D., 2009. Water transports through the four main straits around the South China Sea. Chin. J. Oceanol. Limnol. 27, 229–236.
Wang, G., Su, J., Ding, Y., Chen, D., 2007. Tropical cyclone genesis over the South China Sea. J. Mar. Syst. 68, 318–326.
Wang, C., Wang, X., 2013. Classifying El Niño Modoki I and II by different impacts on rainfall in southern China and typhoon tracks. J. Clim. 26, 1322–1338.
Wang, C., Wang, W., Wang, D., Wang, Q., 2006. Interannual variability of the South China Sea associated with El Niño. J. Geophys. Res.: Oceans 111, C03023.
Wang, B., Wu, R., Fu, X., 2000. Pacific–East Asian teleconnection: How does ENSO affect East Asian climate? J. Clim. 13, 1517–1536.
Wang, D., Xie, Q., Du, Y., Wang, W., Chen, J., 2002. The 1997–1998 warm event in the South China Sea. Chin. Sci. Bull. 47 (14), 1221–1227.
Wang, B., Zhang, Q., 2002. Pacific–East Asian teleconnection. Part II: How the Philippine Sea anomalous anticyclone is established during El Niño development? J. Clim. 15, 3252–3265.
Warner, J.C., Armstrong, B., He, R., Zambon, J.B., 2010. Development of a Coupled Ocean-Atmosphere-Wave-Sediment Transport (COAWST) modeling system. Ocean Model. 35, 230–244.
Wu, C.R., Hsin, Y.C., 2005. Volume transport through the Taiwan Strait: A numerical study. Terr. Atmos. Ocean. Sci. 16, 377–391.
Wu, R., Kirtman, B.P., Pegion, K., 2006. Local air–sea relationship in observations and model simulations. J. Clim. 19, 4914–4932.
Wu, B., Zhou, T., Li, T., 2017a. Atmospheric dynamic and thermodynamic processes driving the western North Pacific anomalous anticyclone during El Niño. Part I: Maintenance mechanisms. J. Clim. 30, 9621–9635. http://dx.doi.org/10.1175/JCLI-D-16-0489.1.
Wu, B., Zhou, T., Li, T., 2017b. Atmospheric dynamic and thermodynamic processes driving the western North Pacific anomalous anticyclone during El Niño. Part II: Formation processes. J. Clim. 30, 9637–9650. http://dx.doi.org/10.1175/JCLI-D-16-0495.1.
Xiao, F., Zeng, L., Liu, Q.Y., Zhou, W., Wang, D., 2018. Extreme subsurface warm events in the South China Sea during 1998/99 and 2006/07: observations and mechanisms. Clim. Dyn. 50 (1–2), 115–128.
Xie, S.-P., Chang, C.H., Xie, Q., Wang, D., 2007. Intraseasonal variability in the summer South China Sea: Wind jet, cold filament, and recirculations. J. Geophys. Res. 112, C10008. http://dx.doi.org/10.1029/2007JC004238.
Xie, S.P., Hu, K., Hafner, J., Tokinaga, H., Du, Y., Huang, G., Sampe, T., 2009. Indian Ocean capacitor effect on Indo–western Pacific climate during the summer following El Niño. J. Clim. 22, 730–747.
Xu, F.H., Oey, L.Y., 2014. State analysis using the Local Ensemble Transform Kalman Filter (LETKF) and the three-layer circulation structure of the Luzon Strait and the South China Sea. Ocean Dyn. 64, 905–923.
Yang, Q., Tian, J., Zhao, W., 2010. Observation of Luzon Strait transport in summer 2007. Deep-Sea Res. I 57 (5), 670–676.
Yang, Y., Xie, S.P., Du, Y., Tokinaga, H., 2015. Interdecadal difference of interannual variability characteristics of South China Sea SSTs associated with ENSO. J. Clim. 28, 7145–7160.
Yaremchuk, M., McCreary, Jr., J., Yu, Z., Furue, R., 2009. The South China Sea throughflow retrieved from climatological data. J. Phys. Oceanogr. 39, 753–767.
Yaremchuk, M., Qu, T., 2004. Seasonal variability of the large-scale currents near the coast of the Philippines. J. Phys. Oceanogr. 34, 844–855.
Yuan, D., Han, W., Hu, D., 2006. Surface Kuroshio path in the Luzon Strait area derived from satellite remote sensing data. J. Geophys. Res.: Oceans 111, C11007.
Yuan, Y., Tseng, Y.H., Yang, C., Liao, G., Chow, C.H., Liu, Z., Zhu, X.H., Chen, H., 2014. Variation in the Kuroshio intrusion: Modeling and interpretation of observations collected around the Luzon Strait from 2009 to 2011. J. Geophys. Res.: Oceans 119, 3447–3463.
Zhang, R., Sumi, A., Kimoto, M., 1999. A diagnostic study of the impact of El Niño on the precipitation in China. Adv. Atmos. Sci. 16, 229–241.
Zhao, W., Hou, Y.-J., Qi, P., Le, K.-T., Li, M.-K., 2009. The effects of monsoons and connectivity of South China Sea on the seasonal variations of water exchange in the Luzon Strait. J. Hydrodyn. 21, 264–270.
Zu, T., Xue, H., Wang, D., Geng, B., Zeng, L., Liu, Q., Chen, J., He, Y., 2019. Interannual variation of the South China Sea circulation during winter: intensified in the southern basin. Clim. Dynam. 52 (3–4), 1917–1933.